The 20S proteasome activator PA28γ controls the compaction of chromatin

Didier Fesquet, David Llères, Charlotte Grimaud, Cristina Viganò, Francisca Méchali, Séverine Boulon, Robert Feil, Olivier Coux, Catherine Bonne-Andrea, Véronique Baldin

The 20S proteasome activator PA28γ controls the compaction of chromatin

Authors:

Didier Fesquet[1*], David Llères[2*], Charlotte Grimaud[3], Cristina Viganò[1,4], Francisca Méchali[1], Séverine Boulon[1], Robert Feil[2], Olivier Coux[1], Catherine Bonne-Andrea[1] and Véronique Baldin[1§]

Affiliations:

1 Centre de Recherche de Biologie cellulaire de Montpellier (CRBM), Université de Montpellier, CNRS, 34293 Montpellier, France

2 Institut de Génétique Moléculaire de Montpellier (IGMM), Université de Montpellier, CNRS, 34293 Montpellier, France

3 Institut de Recherche en Cancérologie de Montpellier (IRCM), INSERM U1194, Institut Régional du Cancer (ICM), Université de Montpellier, CNRS Route de Mende, 34293 Montpellier, France

4 Present address: Asst-Monza Ospedale san Gerardo, via Pergolesi 33, 20900 Monza (MB) Italy

*: These authors contributed equally to this work

§ Corresponding author: Véronique Baldin, CRBM-UMR-5237, CNRS, 1919 Route de Mende, 34293 Montpellier cedex 5, Phone: (33) 4 34 35 95 43

E-mail: veronique.baldin@crbm.cnrs.fr

Running title: PA28γ controls chromatin compaction

Key words: PA28γ/ Proteasome/ HP1/ Heterochromatin/ FLIM-FRET.

Abstract

PA28γ, a nuclear activator of the 20S proteasome, is involved in the degradation of several proteins regulating cell proliferation, but its precise cellular functions remain unclear. Here, we show that PA28γ is crucial for chromatin compaction. In human cells, we find that a small fraction of PA28γ co-localizes with HP1β, and PA28γ is present at HP1β-containing repetitive-DNA regions. PA28γ-depletion induces a decompaction of pericentromeric heterochromatin, as observed upon HP1β-knockdown. Using a quantitative FLIM-FRET based microscopy assay monitoring close proximity between nucleosomes in living cells, we show that PA28γ controls chromatin compaction more broadly. Importantly, HP1β on its own is unable to drive chromatin compaction without the presence of PA28γ. At the molecular level, PA28γ is necessary to maintain the level of H3K9 tri-methylation, as well as H4K20 mono- and tri-methylation, modifications required for heterochromatin establishment. Overall, our findings demonstrate the implication of a proteasome regulator in chromatin organization.

Introduction

Proteasome-mediated protein degradation is a central pathway that controls the stability and the function of numerous proteins in most cellular processes (Collins & Goldberg, 2017). The various functions of the proteasome are actually performed by a family of proteasome complexes resulting from the association of different regulators/activators with the catalytic core-called the 20S proteasome (Rechsteiner & Hill, 2005; Coux *et al*., 2020). Among the proteasome family, the best-characterized member is the 26S proteasome, composed of the 20S core proteasome and the 19S regulator, which degrades poly-ubiquitylated proteins in an ATP-dependent manner (Collins & Goldberg, 2017; Bard *et al*., 2018). In the nucleus, two other regulators, PA200 (Ustrell *et al*., 2002; Rechsteiner & Hill, 2005) and the homoheptamer PA28γ (also known as REGγ or Ki antigen) (Ma *et al*., 1992; Wilk *et al*., 2000; Mao *et al*., 2008), are present and function in an ATP- and ubiquitin- independent manner. Among their many functions, it is now well established that proteasome complexes are associated with chromatin and enriched at specific sites in the genome (Geng & Tansey, 2012; Kito *et al*., 2020). Notably, they are specifically recruited during transcription or in response to DNA damage, thereby suggesting a direct role for chromatin-associated proteasome complexes in genomic processes (McCann & Tansey, 2014).

Chromatin exists mainly in two distinct compaction states: whereas euchromatin is a relaxed state that is generally transcriptionally active, heterochromatin corresponds to a highly compacted and often repressed state, rich in repetitive sequences such as satellite repeats, transposable elements and ribosomal DNA (Lippman *et al*., 2004; Nishibuchi & Nakayama, 2014; Saksouk *et al*., 2015; Janssen *et al*., 2018). Heterochromatin is paramount to the stability of eukaryotic genomes. Indeed, loss of control over these repetitive DNA regions can lead to transcriptional perturbation and DNA recombination, all of which events are at the root of oncogenic transformation (Ayarpadikannan & Kim, 2014; Klement & Goodarzi, 2014).

Multiple evidence from genetic and cell biology point to an important involvement of Heterochromatin Protein-1 (HP1) (Maison & Almouzni, 2004; Verschure *et al*., 2005) and trimethylation of histone H3 lysine 9 (H3K9me3) (Martin & Zhang, 2005; Saksouk *et al*., 2015) and of histone H4 lysine 20 (H4K20me3) (Schotta *et al*., 2004; Oda *et al*., 2009; Beck *et al*., 2012; Bosch-Presegue *et al*., 2017) in establishing and maintaining heterochromatic states. Two proteins of the HP1 family (Nielsen *et al*., 2002; Thiru *et al*., 2004), HP1α and β, are recruited through their binding to H3K9me3, and participate in the folding of chromatin

into higher-order structures (Bannister *et al*., 2001; Lachner *et al*., 2001; Maison & Almouzni, 2004; Machida *et al*., 2018). Recent reports identify a liquid phase-like HP1 population that generates a dynamic phase transition compartment surrounding the stable chromatin-bound HP1 fraction (Larson *et al*., 2017; Strom *et al*., 2017). Such a compartmentalization mechanism may facilitate the access of proteins and their rapid exchange, necessary for the dynamic structural changes of heterochromatin during cell cycle progression and in the DNA damage response. Thus, it has been suggested that HP1 would act as a platform that selectively favors local concentration of different proteins to fulfill their chromatin-related functions (Grewal & Jia, 2007). However, the mechanism by which HP1 folds H3K9me3-containing chromatin into higher-order structures, and the requirement of other factors have not been fully elucidated.

The roles of the different proteasome complexes in chromatin organization remain still elusive as well. Although PA28γ-20S proteasome complexes constitute only a minor fraction of the whole proteasome population (below 5%) (Fabre *et al*., 2014), PA28γ is important for cell growth and proliferation. Indeed, among the limited number of identified proteins whose degradation is mediated by PA28γ-20S proteasome complexes, many of these such as CKIs (p21, p19, p16) and Myc (Chen *et al*., 2007; Li *et al*., 2007; Li *et al*., 2015) are involved in the control of cell proliferation. Consistent with this, PA28γ-knockout mice show a decrease in body size (Murata *et al*., 1999; Barton *et al*., 2004). In addition, PA28γ plays a role in intra-nuclear organization, since it is involved in the dynamics of various nuclear bodies, including Cajal bodies (Cioce *et al*., 2006; Jonik-Nowak *et al*., 2018), nuclear speckles (Baldin *et al*., 2008), and promyelocytic leukemia protein bodies (PML) (Zannini *et al*., 2009). A potential role of PA28γ in chromatin has also been proposed, since it has been linked to chromosome stability (Zannini *et al*., 2008) and DNA repair (Levy-Barda *et al*., 2011).

In this study, we highlight a still unsuspected function of PA28γ in the control of chromatin compaction. By studying the localization of the 20S proteasome in human cells, we found that a fraction of the 20S proteasome localizes in nuclear foci, together with its regulator PA28γ and HP1β. Subsequent investigations revealed that PA28γ is associated with repetitive DNA sequences abundant in heterochromatin, and is necessary to sustain the compaction of chromatin. This function of PA28γ, possibly independent of the 20S proteasome, depends on its ability to maintain appropriate levels of H3K9me3 and H4K20me3, histone modifications that are both involved in heterochromatin formation.

Results

A fraction of PA28γ-20S proteasome complexes co-localizes with HP1 proteins.

To investigate the subcellular location of the 20S proteasome in human cells, we established a stable U2OS cell line expressing an inducible alpha 4 (α4) protein, one of the constitutive subunits of the 20S proteasome, fused with GFP (α4-GFP). Biochemical characterization of this cell line demonstrated that the α4-GFP subunit was correctly incorporated into proteolytically active proteasomes (Fig S1A). As reported for the endogenous α4 subunit, ectopic α4-GFP was detected throughout the cell, with an accumulation in the nucleoplasm (Fig 1A). However, it was also present in nuclear foci of a fraction of asynchronously growing cells (~ 25-30%) (Fig 1A-B). A similar location to nuclear foci was observed in U2OS cells expressing an ectopic untagged α4 subunit, thus excluding a potential mis-localization due to the fusion with the GFP moiety (Fig S1B). Co-immunostaining experiments showed that other subunits of the 20S proteasome, such as α6, were detected in α4-GFP foci as well (Fig 1B), reflecting the presence of the entire 20S proteasome. In addition to the 20S proteasome, we detected its PA28γ regulator (Fig 1B), but not the 19S complex, as shown by the absence of accumulation of the 19S subunit Rpt6 within α4-GFP foci (Fig 1B). Interestingly, PA28γ-containing α4-GFP foci were resistant to an extraction-fixation buffer treatment (Fig 1C), used to reveal chromatin-associated proteins by immunofluorescence (Britton *et al*., 2013). These observations suggest that α4-GFP foci are closely linked to chromatin. Combined, these findings reveal a particular nuclear localization of PA28γ-20S proteasome complexes upon ectopic expression of α4 subunit.

Visualization of α4-GFP in living U2OS cells by time-lapse video microscopy revealed that these α4-GFP nuclear foci are dynamic, as their presence fluctuates throughout the cell cycle (Movie-1). α4-GFP displayed a diffused localization during mitosis, after which it started to assemble into foci, whose number and size gradually increased during interphase. Detection of nuclear α4-GFP foci in synchronized cells indicated that the percentage of cells with α4-GFP foci reached a peak in late-S/early-G2 phases (Fig S1C).

Next, we investigated the nature of the α4-GFP nuclear foci. Among different proteins forming nuclear foci, we focused our attention on a member of the HP1 family, HP1β. Newly synthetized HP1β was reported to also accumulate into nuclear foci with a characteristic peak in late-S/early-G2 phases when GFP-HP1β was overexpressed (Dialynas *et al*., 2006). By

performing immunostaining against HP1β protein, we revealed the presence of endogenous HP1β in α4-GFP foci (Fig 1D). Immunoblot analyses of PA28γ and GFP immunoprecipitation experiments performed in U2OS-α4-GFP cell extracts showed that HP1β is present in PA28γ- and 20S proteasome-containing complexes (Fig 1E). We then wondered whether HP1β plays a role in the formation of PA28γ-20S proteasome foci. After depletion of HP1β by siRNAs in U2OS-α4-GFP cells (Fig 1F), we observed a significant decrease of the percentage of cells containing α4-GFP foci (~14%) compared to the control cells (~36%) (Fig 1F, bar graph). We also noted that PA28γ was no longer detected at identifiable nuclear foci in the absence of HP1β. Importantly, PA28γ depletion significantly decreased the percentage of cells containing α4-GFP foci (~9.7%) (Fig 1F), suggesting that PA28γ is required for their formation. First, these results indicate that HP1β plays a role in the recruitment and/or retention of PA28γ-20S proteasome to these foci when α4 is over-expressed. Second, these data reveal that PA28γ is required to recruit the 20S proteasome to nuclear foci.

Altogether, the above findings demonstrate that ectopic α4 overexpression promotes the enrichment of PA28γ-20S proteasome complexes in HP1β-containing nuclear foci.

Without α4 overexpression, a fraction of PA28γ co-localizes also with HP1β.

Immunostaining analyses of PA28γ in U2OS cells revealed only a diffuse distribution of PA28γ within the nucleus. We hypothesized that the presence of foci was due to the amplification of a natural process that most likely occurs in cells, but was only easily detectable when exacerbated by α4 overexpression. To test this hypothesis, we asked whether PA28γ co-localizes with HP1 proteins in U2OS cells without α4 ectopic expression.

Since both PA28γ and HP1β proteins are abundant in the nucleus, we pre-extracted the soluble nuclear proteins by treating the U2OS cells with 0.5%Triton X-100/PBS (Guillot *et al*., 2004), and performed immunostaining of HP1β and PA28γ proteins. Analysis of widefield microscope images (Figs 2A and S2A) showed a potential co-localization between HP1β and PA28γ in some discrete areas of the nucleus (Fig 2A, merge image and higher magnifications). Z-stack acquisition on an Airyscan confocal microscope (Fig 2B, left panel), followed by image analysis with Imaris software module, confirmed the co-localization between both proteins in U2OS cells (~32 co-localization sites per nucleus) (Fig 2B, right panel).

To strengthen this result, we used the *in situ* Proximity-Ligation Assay (*is*-PLA), which allows the detection of the close proximity between two proteins within cells (less than 40 nm, i.e. likely to be an interaction) (Soderberg *et al*., 2006). Using both PA28γ and HP1β antibodies, *is*-PLA revealed a characteristic dotted pattern throughout the nuclei of U2OS cells (Fig 2C, upper middle panel), strongly supporting the close proximity of the two proteins. Silencing of PA28γ expression with siRNAs (Fig 2C, left panel), used as a negative control, abolished the PLA dots, demonstrating the specificity of the PLA signal (Fig 2C, lower middle panel). Quantification of the number of PLA dots per nucleus (see Materials and methods) indicated on average 37 and 1.4 dots per nucleus, in the presence and absence of PA28γ, respectively (Fig 2C, bar graph). We also evidenced that PA28γ co-localizes in part with HP1α (Fig S2B). Finally, we also found a close proximity between the 20S proteasome and HP1β by *is*-PLA, using antibodies against the α4 subunit of the 20S proteasome (Fig 2D).

Recently, we identified an important regulator of PA28γ, the protein PIP30 (PSME3IP1), which affects PA28γ interactions and localization in Cajal bodies (Jonik-Nowak *et al*., 2018). Since PIP30 was detected in α4-GFP foci, we tested whether PIP30 modulates the co-localization of PA28γ and HP1β. We found that PIP30 had no effect on this process since no difference in the number of PLA-dots between PA28γ and HP1β was observed in wild-type and PIP30-knockout (KO-PIP30) U2OS cells (Fig S2D).

Taken together, these results demonstrate that a fraction of PA28γ and the 20S proteasome is in close physical proximity (and thus is likely to interact either directly or indirectly) to a fraction of the heterochromatin-binding protein HP1β.

PA28γ controls pericentromeric heterochromatin compaction.

The co-localization of PA28γ and HP1β prompted us to investigate whether PA28γ was associated with chromatin comprising repetitive sequences characteristic of heterochromatin, such as interspersed (HERV-K), pericentromeric (Satellite II and α Satellite) and Major Satellite (L1 LINE) DNA repetitive sequences (Padeken *et al*., 2015). Quantitative chromatin immunoprecipitation (ChIP-qPCR) experiments performed on parental (WT) *versus* KO-PA28γ U2OS cells revealed that PA28γ was associated with all four heterochromatin sequences tested (Fig 3A), as was HP1β (Fig S3). Note that PA28γ is also associated with a DNA sequence corresponding to Cyclin E2 promoter, located in euchromatin (Fig 3A).

Based on these results, we then investigated whether PA28γ could regulate heterochromatin compaction. For this purpose, we used a previously described U2OS cell clone (F42B8) carrying *lacO* DNA repeats stably integrated within constitutive heterochromatin, at a pericentromeric region (Jegou *et al*., 2009). This *lacO* array forms a single heterochromatic locus that can be visualized in cells following the transient expression of the GFP-LacI construct. The GFP signal allows us to measure the area occupied by the *lacO* locus and thus to quantify the variations of its compaction state. We first examined the effect of HP1β depletion on *lacO* array compaction by transfecting these cells with siRNAs directed against HP1β (si-HP1β) or luciferase (si-Luc), and with a GFP-LacI-expressing construct. The efficiency of si-HP1β was verified by immunoblot (Fig 3B, upper panel), and changes in heterochromatin compaction state were monitored 48 hours post-transfection by fluorescence microscopy (Fig 3B, lower panel). *LacO* locus appeared as a small dot with a surface area that was not significantly affected by the transfection of si-Luc (0.390 ± 0.045 μm^2 *vs* 0.370 ± 0.052 μm^2 in control cells). Upon HP1β knockdown, we observed a significant increase of the GFP-LacI dot surface area (0.730 ± 0.069 μm^2). This corresponds to an expansion of the surface area occupied by the *lacO* DNA repeats due to heterochromatin decompaction (Fig 3C). We then examined the effect of PA28γ knockdown (Fig 3D-E). Upon PA28γ-depletion we observed a significant increase in the GFP-LacI dot surface area (0.636 ± 0.014 μm^2 *vs* 0.370 ± 0.052 μm^2 and 0.443 ± 0.011 μm^2 in control cells and si-Luc treated cells, respectively) (Fig 3E). Thus, as observed in absence of HP1β, the pericentromeric heterochromatin is significantly decompacted in the absence of PA28γ.

PA28γ controls chromatin compaction in living cells, independently from its interaction with the 20S proteasome.

To complete and expand the results obtained on fixed cells and at a specific genome locus, we performed quantitative FLIM-FRET (Fluorescence Lifetime Imaging Microscopy-Förster Resonance Energy Transfer) measurements of chromatin compaction at the nanometer-scale in a single living cell. For this study, we used HeLa cells that stably co-expressed histone H2B-GFP and mCherry-H2B ($HeLa^{H2B\text{-}2FPs}$). FRET was measured between the fluorophore-tagged histones incorporated into the chromatin and in this assay an increase in FRET efficiency corresponds to an increase in the occurrence of close proximity (<10 nm) between nucleosomes (Lleres *et al*., 2009).

We first confirmed the co-localization between PA28γ and HP1β proteins at some nuclear sites in HeLa cells as seen in U2OS cells, by using *is*-PLA (Fig S4). Then, we established a stable CRISPR/Cas9 PA28γ knockout HeLa cell line (Fig 4A), expressing either H2B-GFP alone (HeLa$^{H2B\text{-}GFP}$-KO-PA28γ) or both H2B-GFP and mCherry-H2B (HeLa$^{H2B\text{-}2FPs}$-KO-PA28γ). We verified that PA28γ depletion affected neither H2B-GFP nor mCherry-H2B expression levels by immunoblot and microscopy analysis (Fig S5A-B).

Next, we analyzed by FLIM-FRET microscopy the levels of nanoscale chromatin compaction in asynchronous interphase parental and KO-PA28γ cells. In wild-type (WT) HeLa$^{H2B\text{-}2FPs}$ cells, a heterogeneous FRET efficiency map was apparent throughout nuclei on representative images using continuous pseudocolors (Fig 4B, left panel). We found that the areas with highest FRET signal (red-orange population) decreased in KO-PA28γ cells (Fig 4B, left panel). This effect was confirmed by the determination of the mean FRET efficiency percentage, which shows a major reduction in the level of chromatin compaction compared to the WT cells (Fig 4B, right panel). As a positive control for chromatin decompaction, we treated HeLa$^{H2B\text{-}2FPs}$ cells with Trichostatin A (TSA), an inhibitor of histone deacetylases used to provoke large-scale chromatin decompaction (Lleres *et al*., 2009; Otterstrom *et al*., 2019). As expected, after 24 hours of TSA treatment, the mean FRET efficiency percentage dropped drastically, consistent with a massively decompacted interphase chromatin (Fig S5C). By extracting the FRET efficiency distribution curves related to the FRET efficiency map of individual nuclei in both WT and KO-PA28γ cell lines, we observed upon loss of PA28γ a marked reduction of the high FRET population corresponding to high levels of chromatin compaction (Fig 4C, black curve *vs* blue curve). In contrast, the low-FRET population corresponding to chromatin regions with the lowest degree of chromatin compaction remained poorly affected. Therefore, PA28γ seems to impact preferentially, if not exclusively, the most condensed chromatin domains during interphase. To ascertain that the relaxation of the chromatin was due to the absence of PA28γ in the above experiments, we re-expressed PA28γ in PA28γ-KO cells (two different clones named KO/KI-WT#6 and # 8 were selected) at a level comparable to that of the endogenous protein (Fig S5D). Remarkably, for KO/KI-WT#6 and # 8 clones, the FRET efficiency was restored to values similar to WT cells (Fig 4D) indicating the re-establishment of normal chromatin compaction. Thus, these results show that PA28γ plays an important role in regulating the compaction of chromatin in cells, with a particular impact on the highly structured chromatin.

An important question was to determine whether the 20S proteasome is required for this function of PA28γ. For this, we used a mutant of PA28γ deleted of its last C-terminal 14 amino acids (called ΔC), which is unable to bind and therefore to activate the 20S proteasome (Ma *et al*., 1993; Zannini *et al*., 2008). We stably expressed this mutant in HeLa$^{H2B\text{-}2FPs}$-KO-PA28γ cells (named KO/KI-ΔC) at an expression level comparable to that observed in WT cells (Fig S5E). The inability of this PA28γ mutant to bind the 20S proteasome was confirmed by co-immunoprecipitation experiments from cell extracts treated (Fig 4E) or not (Fig S5F) with the proteasome inhibitor MG132, known to increase the association between PA28γ and the 20S proteasome (Welk *et al*., 2016). As shown in Fig 4E and S5F, the 20S proteasome was detected by the presence of its α4 subunit in PA28γ immunoprecipitations from HeLa$^{H2B\text{-}2FP}$ WT and KO/KI-WT cell extracts, but not in KO/KI-ΔC and KO-PA28γ cells. Chromatin compaction was then analyzed by FLIM-FRET in living asynchronous cells. Surprisingly, we found that the expression of PA28γ-ΔC mutant restored the level of chromatin compaction in PA28γ-KO cells to a FRET efficiency value (24.7%) similar to the one observed in WT cells (23.03%) (Fig 4F). These results demonstrate that the compaction of chromatin requires PA28γ, but not its interaction with the 20S proteasome.

PA28γ is required for HP1 to mediate chromatin compaction.

To further characterize the PA28γ/HP1β connection, we performed siRNA-mediated depletion of both PA28γ and HP1β proteins (Fig 5A), and analyzed the effects on chromatin compaction levels by FLIM-FRET. FRET measurements revealed a marked decompaction of chromatin upon PA28γ-knockdown that was even stronger than upon HP1β depletion (Fig 5B). This decompaction was correlated with the clear disappearance of the most compacted states of the chromatin within nuclei (Fig 5C, left panel). To complete these data, the quantitative analysis of the FRET distribution profiles revealed a less pronounced decompaction of the chromatin with still some remaining high-FRET values upon si-HP1β depletion than after si-PA28γ depletion (Fig 5C right panel, compare red and black curves). Most likely the lower effect of HP1β knockdown can be explained by the presence of HP1α and/or by the redundancy of the HP1 isoforms in regulating chromatin compaction (Bosch-Presegue *et al*., 2017). Importantly, these results indicate that even in the presence of HP1 proteins the lack of PA28γ results into a strong decompaction of chromatin. We noted that the transfection of the siRNA-Luc only (blue curve) caused an increase in the high-FRET population (Fig 5C right panel) as compared to parental cells (Fig 4C right panel).

Intriguingly, we noted that PA28γ-knockdown by siRNA had a stronger effect than the PA28γ-knockout. This difference can be explained by potential compensatory mechanisms developed by the PA28γ-KO cell line to maintain homeostasis. Finally, depletion of both PA28γ and HP1β had no additional effect compared to PA28γ alone. Altogether, these results demonstrate that PA28γ and HP1β control the compaction of the chromatin, and that PA28γ is required for this process to occur properly.

In order to determine the impact of chromatin decompaction induced by PA28γ depletion on physiological events, we next investigated the consequences of PA28γ depletion on the cell cycle. Analysis of cell-cycle profiles of KO-PA28γ cells by fluorescence-activated cell sorting (FACS) revealed a minor but significant increase of 10% in the number of G1-phase cells, and a decrease of 7% in the number of S-phase cells relative to WT cells (Fig S6A), as previously described in PA28γ$^{-/-}$ MEFs (Murata *et al*., 1999). To obtain more insight into these perturbations, we analyzed the progression of both cell lines during the cell cycle after their release from a G1/S boundary block induced by double thymidine treatment. As shown in Fig S6B, the depletion of PA28γ in U2OS cells caused an early exit from S phase (left panel) correlated to an early entrance in G2 phase as compared to the parental U2OS cells (right panel). This significant shortening of S phase (≈ 1 hour) in KO-PA28γ cells was also confirmed by an immunoblot using cell cycle markers including Cyclin E and the phosphorylation of histone H3 on serine 10 (Fig S6C). Together, these results indicate that the duration of S phase is reduced in the absence of PA28γ, suggesting that the chromatin decompaction induced by the lack of PA28γ could facilitate the accessibility to DNA for the replication machinery.

PA28γ contributes to the maintenance of heterochromatin marks.

Besides the recruitment of HP1 proteins, methylations of histone H3 on lysine 9 (H3K9me) (Maison & Almouzni, 2004; Trembecka-Lucas *et al*., 2013; Saksouk *et al*., 2015) and histone H4 on lysine 20 (H4K20me) (Shoaib *et al*., 2018) have been shown to be important for chromatin compaction. Since tri-methylation of histone H4 (H4K20me3) is also an evolutionarily-conserved mark of heterochromatin (Schotta *et al*., 2004; Balakrishnan & Milavetz, 2010; Beck *et al*., 2012), we tested whether PA28γ regulates these heterochromatin-enriched modifications. By analyzing the levels of H3K9me3 in total cell extracts by immunoblotting, no change in the steady-state level of H3K9me3 was observed in KO-PA28γ

cells compared to WT cells (Fig 6A). By contrast, PA28γ depletion led to a decrease (~20%) in the steady-state level of H4K20me3 (Fig 6B). This result was particularly interesting since it has recently been suggested that HP1β mediates a direct functional link with H4K20me3 (Bosch-Presegue *et al*., 2017). As H4K20me3 depends on the mono-methylation of histone H4 lysine K20 (H4K20me1) (Tardat *et al*., 2007), we also analyzed the steady-state level of H4K20me1. We observed a strong reduction of H4K20me1 (~40%) (Fig 6B). To examine the variation of H3K9me3 and H4K20me3 at specific heterochromatin sequences, we carried out ChIP assays on parental (WT) and KO-PA28γ U2OS cells using antibodies against H3K9me3 and H4K20me3, and performed qPCR using the same primers as in Fig 3A. We observed a significant decrease in H3K9me3 precipitation levels at these specific sequences (Fig 6C) that was not detected by immunoblot analyses on total cell extract (Fig 6A). Note that the difference observed between immunoblot and ChIP assay could result from the use of different antibodies in the two experiments and/or be due to the highly enrichment of H3K9me3 in pericentric heterochromatin. We confirmed the decrease of H4K20me3 (≥ 60%) in KO-PA28γ *versus* WT U2OS cells (Fig 6D). As expected, this effect was stronger than the one found in total extract. As summarized in Fig 6E, our data suggest that PA28γ participates to the regulation of histones H3K9 and H4K20 methylation states that are required for heterochromatin establishment.

Discussion

The key finding of this study is that PA28γ, known as a nuclear activator of the 20S proteasome, is an essential factor in the process of chromatin compaction.

We demonstrate that PA28γ plays a key role in this process by showing that: i) the lack of PA28γ causes the decompaction of *lacO* DNA repeats that are stably integrated into pericentromeric heterochromatin, as does the loss of HP1β, ii) the depletion of PA28γ induces a decompaction of the highly structured fraction of the chromatin, even in the presence of HP1 proteins, as visualized in living cells with the quantitative FLIM-FRET measurements of chromatin compaction. In line with these observations, we also found that PA28γ knockout decreases significantly the level of H3K9 and H4K20 tri-methylation, as well as mono-methylation of H4K20.

Importantly, our data show that in interphase PA28γ and HP1β are both required to control the most condensed states of chromatin as defined by our experimental approaches. Whether PA28γ and HP1β act independently or in concert will need further investigation. Nevertheless, based on our data obtained in α4-GFP expressing cells, HP1β seems to be required for the recruitment of PA28γ-20S proteasome complexes in nuclear foci. We show that a fraction of PA28γ and HP1β co-localize in normal cells, although this co-localization is difficult to detect, probably because they are located in much more dynamic and/or transient structures than when α4 is overexpressed. It is thus tempting to speculate that the formation of these foci is an early step in the chromatin condensation process.

Using cells overexpressing α4-GFP, we found that PA28γ-20S proteasome complexes gradually concentrate into foci through mid-to-late S-phase to G2-phase, which is reminiscent of the accumulation of newly-synthetized GFP-HP1β at heterochromatin foci, whose formation has been shown to require passage through S-phase (Dialynas *et al.*, 2006). Interestingly, we found that the loss of PA28γ decreases the S phase duration by one hour. Considering this point, it is tempting to hypothesize that, following the progression of replication forks, PA28γ might regulate the re-establishment of modifications on the newly incorporated histones on each of the daughter DNA strands. To support this hypothesis, in the absence of PA28γ, a significant decrease of H3K9me3 and H4K20me3 marks was observed by ChIP-qPCR experiments at specific heterochromatin regions. Furthermore, an important decrease in the steady-state level of H4K20me1 was found. In addition, the longer G1-phase observed upon the loss of PA28γ is a cell cycle effect comparable to the G1-to-S phase

transition delay reported upon a drop in H4K20me levels (Evertts *et al*., 2013) or upon the depletion of the methyltransferase PR-Set7 (Liao *et al*., 2018). Altogether these data argue for a possible role of PA28γ in the regulation of these histone marks. At this stage it is important to note that the 20S proteasome, which bears the proteolytic activity, is not necessary for PA28γ-mediated chromatin compaction; this precludes any direct regulation of this process by a PA28γ-dependent proteolysis event. PA28γ could potentiate the function of the lysine methyltransferases Suv39h, PR-Set7 or Suv4-20h, which are responsible for H3K9 tri-methylation, H4K20 mono-methylation and H4K20 tri-methylation, respectively. It cannot be excluded that PA28γ could facilitate the action of specific histone deacetylases (HDACs) (Almouzni & Cedar, 2016) and/or the recruitment of chromatin remodeling factors.

Interestingly, recent studies show that HP1 proteins have the capacity to form liquid-like droplets resulting from a liquid-liquid phase separation (LLPS) mechanism (Larson *et al*., 2017; Strom *et al*., 2017). This property could facilitate the enrichment of transient supramolecular complexes/machineries that could rapidly assemble and disassemble, and exchange their components. This plasticity in their composition allows them to efficiently respond to the structural changes of heterochromatin, and might thus stimulate PA28γ's interactions with other proteins required for controlling chromatin compaction. In this context, it is important to underline that PA28γ is involved in the dynamics of various membraneless nuclear bodies (Cioce *et al*., 2006; Baldin *et al*., 2008; Zannini *et al*., 2009; Jonik-Nowak *et al*., 2018), also considered to be liquid-like protein droplet organelles (Erdel & Rippe, 2018; Sawyer *et al*., 2019).

The reason behind the recruitment of 20S proteasome into foci is still an intriguing open question, since its interaction with PA28γ is not required for PA28γ-mediated chromatin compaction. To explain the 20S proteasome recruitment, one possibility is that the catalytic activity of PA28γ-20S proteasome complexes is involved in specific steps of chromatin compaction, such as the control of heterochromatin spreading, as it was shown for the 26S proteasome in yeast (Seo *et al*., 2017). Another possibility, in line with a possible link with LLPS droplet organelle formation (Sawyer *et al*., 2019), is that the recruitment of the 20S proteasome by PA28γ could constitute a reservoir of active proteasome that can rapidly be mobilized upon cellular stress. In the cellular response to DNA double-strand breaks (DSBs), PA28γ is required for the rapid mobilisation of the 20S proteasome at DNA damage sites and contributes to the repair-pathway choice (Levy-Barda *et al*., 2011). In this regard, HP1β was also shown to be recruited at DSB sites and to favor the initiation of DNA damage response

(DDR) by promoting chromatin changes (Ayoub *et al*., 2008; Luijsterburg *et al*., 2009; Bartova *et al*., 2017), it would therefore be interesting to investigate whether the mobilization of PA28γ to DNA damage sites is also dependent on the presence of HP1β.

It is noteworthy that, over the years, PA28γ has been implicated in several chromatin-related processes, such as maintenance of chromosomal stability (Zannini *et al*., 2008), DNA repair (Levy-Barda *et al*., 2011) and control of rDNA transcription (Sun *et al*., 2016). Our present observations suggest that the role of PA28γ in the regulation of chromatin compaction could be the common mechanism that links these processes to PA28γ. Although much remains to be understood regarding the biological functions of PA28γ in this process, our data reveal that PA28γ is a crucial factor in the regulation of chromatin compaction and this discovery undoubtedly opens new perspectives for a deeper understanding of the proteasome functions and the complex mechanisms that control chromatin organization, particularly during cell cycle.

Materials and methods

Plasmids

A human cDNA encoding the full length of 20S proteasome subunit α4 (*PSMA7*), with or without a final stop codon, was PCR amplified from a human fibroblast cDNA library and inserted into $pcDNA_3$ or pML1-EGFP (Baldin *et al*., 2008; Farras *et al*., 2008; Le Feuvre *et al*., 2009). The cDNA encoding α4-EGFP was then inserted into the pTRE2 vector (Clontech). The human HP1β (*CBX1*) cDNA was PCR-amplified from pDONR223 (provided by the Montpellier Genomic Collections facility, IGMM, Montpellier, France) and cloned into pEGFP-C1 (Clontech). For Cas9-mediated gene disruption, guide RNA (GGAAGTGAAGCTCAAGGTAGCGG) targeting PA28γ (*PSME3*) was selected using ChopChop (https://chopchop.rc.fas.harvard.edu/index.php) and oligonucleotides were subcloned into pMLM3636 (a gift from Keith Joung, Addgene plasmid #43860) and pUC57-U6 (a gift from Edouard Bertrand's laboratory, IGMM, Montpellier, France). For rescue experiments, PA28γ ORF WT or delta C-terminal 14 amino acids (called ΔC) were cloned in pSBbi-Pur (gift from E. Kowarz addgene plasmid #60523) according to (Kowarz *et al*., 2015). The resulting vector was co-transfected with pCMV(CAT)T7-SB100 (gift from Zsuzsanna Izsvak, Addgene plasmid #34879) into recipients cells, and puromycin-resistant single colonies were selected for re-expression of PA28γ WT or ΔC proteins. pEGF-LacI (Jegou *et al*., 2009) was a generous gift from Prof. K. Rippe (DKFZ, Heidelberg, Germany).

Antibodies

The following antibodies were used at 1:1000 dilution for immunoblotting and 1-3 μg/ml for immunoprecipitation: anti-PA28γ (rabbit polyclonal BML-PW8190), anti-α4 (1:2000), anti-α6 (1:2000), and anti-Rpt6/Sug1 (mouse monoclonal, BML-PW8120, BML-PW8100 and BML-PW9265, ENZO Life Sciences, respectively); anti-PA28γ (mouse monoclonal, 611180, BD Transduction); anti-HP1α (rabbit polyclonal, 2616S, Cell Signaling); anti-HP1β (rabbit monoclonal (D2F2), 8676S, Cell Signaling, mouse monoclonal (1MOD-1A9) 39979, Active Motif); anti-MCM7 (monoclonal, sc-9966, Santa-Cruz); anti-PIP30 (PSME3IP1) (Jonik-Nowak *et al*., 2018); anti-GFP (mouse monoclonal (Clone 7.1), 11814460001, ROCHE, Sigma); anti-RFP (rat monoclonal, 5F8, Chromotek); anti-β-actin (rabbit monoclonal, 13E5, Cell Signaling); anti-H3K9me3 (mouse monoclonal (clone 2AG-6F12-H4) 39285, Active Motif); anti-H3 (rabbit polyclonal, ab1791, Abcam); anti-H4K20me1 (rabbit polyclonal,

#9724, Cell Signaling Technology); anti-H4K20me3 (rabbit monoclonal, #5737, Cell Signaling Technology); anti-α -tubulin (mouse monoclonal, T9026, Sigma-Aldrich, 1:6,000). Fluorescent secondary antibodies conjugated either to Alexa Fluor 488, 594 and 680 (1:1,000), or to DyLight 680 and 800 (1:10,000) were purchased from Thermo Fisher Scientific. Secondary antibodies conjugated to HRP were purchased from Bio-Rad SA (1:10,000). GFP-TRAP-A® beads were from ChromoTek.

Cell culture, transfections, cell synchronization and FACS analysis

HeLa (CCL-2) and U2OS (HTB-96) cells, obtained from ATCC, were grown in DMEM (Lonza) containing 4.5 g/L glucose, 10% heat-inactivated fetal bovine serum (Biowest), 2 mM glutamine, 100 U/ml penicillin and 10 μg/ml streptomycin (Lonza). A U2OS Tet-Off stable inducible cell line expressing α4-GFP was established as previously described for α7-GFP (Baldin *et al*., 2008), and cultured in medium supplemented with 250 μg/ml G418 (Sigma), 200 μg/ml hygromycin B (Calbiochem) and 2 μg/ml tetracycline (Sigma-Aldrich) to inhibit the expression of the exogenous protein. Single clones were then expanded and analyzed by western blotting using GFP or α4 antibodies. After cell washing with PBS (4 times), α4-GFP expression was induced for 24 to 36 hours in fresh medium, in the absence of tetracycline. For positive clones, the functionality of α4-GFP was controlled by testing its incorporation into the 20S, and the activity of these chimeric 20S proteasomes in a proteasome activity assay (see Appendix Fig S1 B-D). U2OS-LacO (F42B8) cells (a generous gift of Prof. K. Rippe, DKFZ, Heidelberg, Germany) were grown in the same media as U2OS but containing G418 (500 μg/ml) (Jegou *et al*., 2009). Establishment and characterization of parental $HeLa^{H2B\text{-}GFP}$ and $HeLa^{H2B\text{-}2FPs}$ (H2B-GFP and mCherry-H2B) cell lines were previously described (Lleres *et al*., 2009). Of note: after thawing, cells were cultured for one week before seeding, for all experiments.

For transient PA28γ and HP1β knockdown experiments, U2OS and/or HeLa (H2B-GFP or 2FPs) cells were transfected with 20 nM of Luciferase targeting siRNA (si-Luc, 5'-CGTACGCGGAATACTTCGA-3') used as negative control, or -PA28γ (*PSME3*), and -HP1β (*CBX1*) targeting siRNA (si-PA28γ: 5'-GAAUCAAUAUGUCACUCUA-3'; si-HP1β: 5'-AGGAAUAUGUGGUGGAAAA-3') purchased from Eurofins Genomics, using Lipofectamine RNAiMAX (Thermo Fisher Scientific) and examined after 2 days. When indicated, cells were transiently transfected with 0.5 μg/ml DNA using JetPEI™ (Ozyme), according to the manufacturer's instructions and analyzed after one day. Stable U2OS (Jonik-

Nowak *et al*., 2018), HeLa$^{H2B\text{-}GFP}$- and HeLa^{2FPs}-KO-PA28γ cell lines were generated by co-transfection of PSME3/PA28γ sgGuide and pX459 vectors (a gift from Feng Zhang, Addgene plasmid #62988), and cells were selected with puromycin (1 μg/ml). Single clones were then expanded and analyzed by western blotting using PA28γ antibodies. Synchronization of cells at G1/S phases transition was performed by hydroxyurea treatment (10 mM, Sigma-Aldrich) for 16 hours. For Fluorescence-Activated Cell Sorting (FACS) analysis, cells were fixed with 70% ethanol and conserved at -20°C. Before analysis, cells were washed with PBS, resuspended in PBS containing RNAse A (1 mg/ml, Sigma-Aldrich) and propidium iodide (10 μg/ml, Sigma-Aldrich) and incubated for 30 min at room. Samples were run on a FACS Calibur (Becton-Dickinson), and data analysis was performed using CellQuest Pro software (Beckton-Dickinson).

Immunofluorescence and is-PLA assays

Cells on coverslips were fixed in 3.7% paraformaldehyde/PBS at room temperature then permeabilized with 0.25% Triton X-100 in PBS for 5 min, followed by an incubation in methanol (100%) at -20°C for 10 min. Note that in some specific experiments, cells were first pre-extracted CSK buffer (10 mM Pipes, pH 7.0, 100 mM NaCl, 300 mM sucrose, and 3 mM MgCl2, 0.7% Triton X-100) to release soluble proteins, then washed with PBS and fixed with 2% PFA (Britton *et al.*, 2013). After washes with PBS, cells were blocked with 1% FCS/PBS for 15 min. Incubation with primary antibodies (anti-PA28γ 1:6,000 for BML-PW8190 or 1:1,000 for 611180); anti-α4, anti-α6, and anti-Rpt6/Sug1 (1:4,000 BML-PW8120, 1:1,000 BML-PW8100 and 1:1,000 BML-PW9265, respectively; anti-HP1α (1:8,000, 2616S); anti-HP1β (1:1,000 8676S and 1MOD-1A9)) was carried out at 37°C for 1 hour in a humidified atmosphere. After washes, cells were incubated with Alexa Fluor conjugated secondary antibodies for 40 min at RT. DNA was stained with 0.1 μg/ml DAPI (4',6-diamidino-2-phenylindole, dihydrochloride, Sigma-Aldrich) solution 5 min at RT, cells were washed twice in PBS and finally once in H_2O. Coverslips were mounted on glass slides using ProLong Gold anti-fade reagent (Thermo Fisher Scientific). For *in situ* proximity ligation assays (*is*-PLA), cells on coverslips were fixed and permeabilized as above. Coverslips were then blocked in a solution provided by the Duolink® kit (Sigma-Aldrich). Cells were then incubated with antibodies as described above. Duolink® *In Situ* PLA Probe Anti-Rabbit MINUS and Anti-Mouse PLUS and Duolink® *In Situ* Detection Reagents (Sigma-Aldrich) were used, according to the manufacturer's instructions. In some specific experiments, cells were

permeabilized prior the fixation with 0.5% Triton X-100 in PBS for 5 min at 4°C for the co-localization between endogenous PA28γ and HP1β in U2OS cells.

Images and Z-stack images were acquired with 63X/1.32 NA or 100X/1.4 NA oil immersion objective lenses using a DM 6000 microscope (Leica). Microphotographs were taken with a 12-bit CoolSnap HQ2 camera. Images were acquired as TIFF files using MetaMorph imaging software (Molecular Devices). For quantitative analyses of PLA dots, Z-stacks were acquired every 0.3 μm (Z step) with a range of 6-7.5 μm. For endogenous detection, images (as a Z stack, slices every 200 nm) were also acquired on a Zeiss LSM 880 point scanning confocal microscope equipped with a 63x Plan-Apochromat 1.4NA oil immersion objective (Zeiss) and using the 488 nm and 561 nm laser lines with the Airyscan detector. The Zeiss Zen black software was used to process the Airyscan raw Images. Co-localization in 3D, between PA28γ and HP1β, was analyzed using the Imaris (Bitplane) co-localization module.

The number of PLA-dots and the size of GFP-LacI dots were detected with ImageJ (1.49v). Specific macros were created to automatically quantify these different parameters. The script allows the creation of a mask of DAPI image to isolate the nucleus of each cell and create a maximum intensity projection (MIP) of the Z-stacks or the image. The mask is used in the MIP to count the number of PLA-dots of each nucleus via an appropriate threshold. The "Analyze Particles" tool of ImageJ was used to calculate the size of each GFP-LacI dots.

FLIM-FRET Microscopy.

FLIM-FRET data were acquired with a Zeiss LSM 780 laser scanning microscope coupled to a 2-photon Ti:Saphire laser (Chameleon Ultra II tunable 680–1080 nm, Coherent) producing 150-femtosecond pulses at 80 MHz repetition rate and a Time Correlated Single Photon Counting (TCSPC) electronics (SPC-830; Becker & Hickl GmbH) for time-resolved detection. Enhanced green fluorescent protein (EGFP) and mCherry fluorophores were used as a FRET pair. The two-photon excitation laser was tuned to 890 nm for selective excitation of the donor fluorophore. The LSM780 microscope is equipped with temperature- and CO_2-controlled environmental black wall chamber. Measurements were acquired in live cells at 37°C, 5% CO_2 with 63x/1.4 oil Plan-Apochromat objective lens. A short-pass 760-nm dichroic mirror was used to separate the fluorescence signal from the laser light. Enhanced detection of the emitted photons was afforded by the use of the HPM-100 module (Hamamatsu R10467-40 GaAsP hybrid PMT tube). The FLIM data were processed using SPCimage software (Becker & Hickl GmbH).

FLIM-FRET analysis

FLIM-FRET experiments were performed in HeLa cells stably expressing H2B-GFP alone ($HeLa^{H2B\text{-}GFP}$) or with mCherry-tagged histone H2B ($HeLa^{H2B\text{-}2FPs}$). 5 x 10^4 cells were seeded in a Fluorodish 35 (FD35-100, World Precision Instruments). For siRNA experiments, 24 hours after seeding, cells were transfected with 20 nM of siRNA (against Luciferase, PA28γ or HP1β) and FLIM-FRET experiments were performed 48 hours later. 30 min prior to imaging, the culture medium was changed to complete DMEM medium without phenol red. An acquisition time of 90 s was set up for each FLIM experiment. The analysis of the FLIM measurements was performed by using SPCImage software (Becker & Hickl, GmbH). Because FRET interactions cause a decrease in the fluorescence lifetime of the donor molecules (EGFP), the FRET efficiency was calculated by comparing the FLIM values obtained for the EGFP donor fluorophores in the presence ($HeLa^{H2B\text{-}2FPs}$) and absence ($HeLa^{H2B\text{-}GFP}$) of the mCherry acceptor fluorophores. FRET efficiency (E FRET) was derived by applying the following equation:

E FRET = 1- (τDA / τD) at each pixel in a selected region of interest (nucleus) using SPCImage software. τDA is the mean fluorescence lifetime of the donor (H2B-EGFP) in the presence of the acceptor mCherry-H2B in $HeLa^{H2B\text{-}2FPs}$ cells and τD is the mean fluorescence lifetime of H2B-EGFP (in the absence of acceptor) in $HeLa^{H2B\text{-}GFP}$ cells. The FRET distribution curves from nuclei were displayed from the extracted associated matrix using SPCImage and then normalized and graphically represented using Microsoft Excel and GraphPad Prism software. For each experiment, FLIM was performed on multiple cells from several independent experiments (see figure legends).

Time-lapse video microscopy

U2OS-α4-GFP cells seeded on a 6-well plate were induced to expressed α4-GFP 24 hours previously, and imaged on an Olympus IX83 microscope with a 40x objective and equipped with an Andor Zyla 4.2 sCMOS camera (van Dijk *et al*., 2018). Both systems were driven by MetaMorph software. Image were then processed with the imageJ package and saved in Avi Format Schneider, C.A., (Schneider *et al*., 2012).

Immunoprecipitation and immunoblotting

For immunoprecipitation of GFP-fusion or endogenous proteins, cells were lysed in lysis buffer (50 mM Tris-HCl, pH 7.5, 150 mM NaCl, 5 mM $MgCl_2$, 1% IGEPAL CA630, 0.5% DOC, 0.1% SDS, 1 mM DTT, 5 mM EDTA, 50 mM NaF and 1 mM Na_3VO_4) in the presence

of complete EDTA-free protease inhibitor cocktail (Roche Life Science) for 20 min at 4°C. Lysates were clarified by centrifugation for 10 min at 10,000 x g and the protein concentration of the supernatant was determined using BSA as a standard (CooAssay protein dosage reagent, Interchim). Total lysate (200 µg) was pre-cleared for 30 min, and immunoprecipitations were performed using either GFP-TRAP beads or the antibodies indicated and protein A or G magnetic beads (Dynal, Lake Success, NY) for 2 hours at 4°C with constant gentle stirring. After several washes, bead pellets were boiled in 2x Laemmli buffer, separated by SDS-PAGE, and subjected to immunoblotting. Note that proteasome activity assay, cells were homogenized in a modified lysis buffer (50 mM Tris-HCl, pH 8.0, 100 mM NaCl, 5 mM $MgCl_2$, 0.5 mM EDTA, 1 mM ATP, 1 mM DTT, 10% Glycerol, 0.5% IGEPAL CA630, 0.3% Triton X-100) in the same.

ChIP-qPCR

ChIP experiments with U2OS were performed as described previously (Brustel *et al*., 2017). Briefly, cells were fixed with 1% formaldehyde (10 min) and quenching was performed with 125 mM Glycine. After a PBS wash, cells were resuspended in buffer A (10 mM Tris-HCl pH 8, 10 mM KCl, 0.25% Triton X-100, 1 mM EDTA, 0.5 mM EGTA) for 5 min on ice. After centrifugation, nuclei were extracted with buffer B (10 mM Tris pH 8, 200 mM NaCl, 1 mM EDTA, 0.5 mM EGTA for 10 minutes on ice. To extract chromatin, nuclei were resuspended in Lysis buffer (10 mM Tris-HCl pH 8, 140 mM NaCl, 0.1% SDS, 0.5% Triton X-100, 0.05% Na-Deoxycholate, 1 mM EDTA, 0.5 mM EGTA). After sonication with EpiShear probe sonicator (Active Motif) to obtain chromatin fragments less than 800 bp, ChIP was performed with 15-30 µg of sheared chromatin incubated with protein A magnetic beads (Invitrogen, Thermo Fisher) coupled with the appropriate antibody, as follows: anti-H3pan (1 µl/ChIP, C15310135 Diagenode), anti-H3K9me3 (2 µl/ChIP, C15410056 Diagenode), anti-H4K20me3 (2 µl/ChIP, C15410207, Diagenode), anti-PA28γ (0.5 µl /ChIP, ENZO Life Sciences). ChIP experiments were performed at least three times from independent chromatin preparations and quantitative PCR analyses of ChIP DNAs were performed using a SYBR green quantitative PCR kit (Invitrogen, Thermo Fisher) and a LightCycler 480 II instrument (Roche) under conditions standardized for each primer set. The amount of DNA in ChIP samples was extrapolated from standard curve analysis of chromatin DNA before immunoprecipitation (input), and values were represented as the ratio between the percentage of input obtained for each antibody to the ones obtained for H3. Primer sets used for qPCR: HERV-K For 5'-TGCCAAACCTGAGGA AGAAGGGAT-3' and HERV-K

Rev 5'-TGCAGGCATTAAACATCCTGGTGC-3', Sat-II For 5'-CCAGAAGGTAATAA GTGGCACAG-3' and Sat-II Rev 5'-CCCTCCTTGAGCATTCTAACTACC-3', α-Sat For 5'-GAAACACTCTTTCTGCACTACCTG-3' and α-Sat Rev 5'-GGATGGTTCAACACT CTTACATGA-3' (Djeghloul *et al*., 2016), L1 Line 5'UTR For 5'-CAGCTTTGAAGA GAGCAGTGG-3' and L1 LINE 5'UTR Rev 5'-GTCAGGGACCCACTTGAGG-3' (Filipponi *et al*., 2013) and CCNE2: For 5'- AAGCGTTAGAA ATGGCAGAAAG-3' and Rev 5'- TCTCTCCCTAATTTACCTGTAGGA-3'.

Statistics

Error bars represent standard deviations unless otherwise noted. Different tests were used to determine significance, and noted in the legend.

Author contribution

VB conceived the project and supervised the study. DF, DL, CG, CV, SB, CBA, and VB performed experiments and analyzed data. FM generated reagents. OC and RF provided conceptual advice on study and interpretation of the data. CBA and VB wrote the article with input from all of the authors.

Conflict of interest

The authors declare that they have no conflict of interest.

Acknowledgements

We thank Prof. Karsten Rippe (Deutsches Krebsforschungszentrum, Heidelberg, Germany) for providing U2OS-LacO (F42B8) cell and the pEGFP-LacI vector, Dr. Philippe Fort for help with statistical analysis, Dr. Nathalie Morin for Airyscan acquisition and helpful discussions and Dr. Eric Julien for helpful discussions; and the Montpellier Ressources Imagerie (MRI) platform, a member of the National Infrastructure France-BioImaging supported by the French National Agency (ANR-10-INSB-04, Investments for the Future). We thank Dr. James Hutchins for checking the scientific English.

Funding

Institutional support was provided by the Centre National de la Recherche Scientifique (CNRS) and the University of Montpellier. This work was also supported by grants from the People Programme (Marie Curie Actions) of the EU Seventh Framework Programme (FP7 REA agreement 290257, UPStream, to OC), Comité de l'Aude et Comité du Gard de la Ligue Nationale Contre le Cancer (2014 and 37-2015, to VB), Fondation ARC pour la Recherche

sur le Cancer (SFI20111203984, to SB/ PJA20181207962, to DL), Institut National du Cancer (INCa) (PLBIO18-KiMec, to RF).

References

Almouzni G, Cedar H. 2016. Maintenance of Epigenetic Information. *Cold Spring Harb Perspect Biol* **8**

Ayarpadikannan S, Kim HS. 2014. The impact of transposable elements in genome evolution and genetic instability and their implications in various diseases. *Genomics Inform* **12:** 98-104.

Ayoub N, Jeyasekharan AD, Bernal JA, Venkitaraman AR. 2008. HP1-beta mobilization promotes chromatin changes that initiate the DNA damage response. *Nature* **453:** 682-686.

Balakrishnan L, Milavetz B. 2010. Decoding the histone H4 lysine 20 methylation mark. *Crit Rev Biochem Mol Biol* **45:** 440-452.

Baldin V, Militello M, Thomas Y, Doucet C, Fic W, Boireau S, Jariel-Encontre I, Piechaczyk M, Bertrand E, Tazi J, Coux O. 2008. A novel role for PA28gamma-proteasome in nuclear speckle organization and SR protein trafficking. *Mol Biol Cell* **19:** 1706-1716.

Bannister AJ, Zegerman P, Partridge JF, Miska EA, Thomas JO, Allshire RC, Kouzarides T. 2001. Selective recognition of methylated lysine 9 on histone H3 by the HP1 chromo domain. *Nature* **410:** 120-124.

Bard JAM, Goodall EA, Greene ER, Jonsson E, Dong KC, Martin A. 2018. Structure and Function of the 26S Proteasome. *Annu Rev Biochem* **87:** 697-724.

Barton LF, Runnels HA, Schell TD, Cho Y, Gibbons R, Tevethia SS, Deepe GS, Jr., Monaco JJ. 2004. Immune defects in 28-kDa proteasome activator gamma-deficient mice. *J Immunol* **172:** 3948-3954.

Bartova E, Malyskova B, Komurkova D, Legartova S, Suchankova J, Krejci J, Kozubek S. 2017. Function of heterochromatin protein 1 during DNA repair. *Protoplasma* **254:** 1233-1240.

Beck DB, Oda H, Shen SS, Reinberg D. 2012. PR-Set7 and H4K20me1: at the crossroads of genome integrity, cell cycle, chromosome condensation, and transcription. *Genes Dev* **26:** 325-337.

Bosch-Presegue L, Raurell-Vila H, Thackray JK, Gonzalez J, Casal C, Kane-Goldsmith N, Vizoso M, Brown JP, Gomez A, Ausio J, Zimmermann T, Esteller M, Schotta G, Singh PB, Serrano L, Vaquero A. 2017. Mammalian HP1 Isoforms Have Specific Roles in Heterochromatin Structure and Organization. *Cell Rep* **21:** 2048-2057.

Britton S, Coates J, Jackson SP. 2013. A new method for high-resolution imaging of Ku foci to decipher mechanisms of DNA double-strand break repair. *J Cell Biol* **202:** 579-595.

Brustel J, Kirstein N, Izard F, Grimaud C, Prorok P, Cayrou C, Schotta G, Abdelsamie AF, Dejardin J, Mechali M, Baldacci G, Sardet C, Cadoret JC, Schepers A, Julien E. 2017. Histone H4K20 tri-methylation at late-firing origins ensures timely heterochromatin replication. *Embo J* **36:** 2726-2741.

Chen X, Barton LF, Chi Y, Clurman BE, Roberts JM. 2007. Ubiquitin-independent degradation of cell-cycle inhibitors by the REGgamma proteasome. *Mol Cell* **26:** 843-852.

Cioce M, Boulon S, Matera AG, Lamond AI. 2006. UV-induced fragmentation of Cajal bodies. *J Cell Biol* **175:** 401-413.

Collins GA, Goldberg AL. 2017. The Logic of the 26S Proteasome. *Cell* **169:** 792-806.

Coux O, Zieba BA, Meiners S. 2020. The Proteasome System in Health and Disease. *Adv Exp Med Biol* **1233:** 55-100.

Dialynas GK, Makatsori D, Kourmouli N, Theodoropoulos PA, McLean K, Terjung S, Singh PB, Georgatos SD. 2006. Methylation-independent binding to histone H3 and cell cycle-dependent incorporation of HP1beta into heterochromatin. *J Biol Chem* **281:** 14350-14360.

Djeghloul D, Kuranda K, Kuzniak I, Barbieri D, Naguibneva I, Choisy C, Bories JC, Dosquet C, Pla M, Vanneaux V, Socie G, Porteu F, Garrick D, Goodhardt M. 2016. Age-Associated Decrease of the Histone Methyltransferase SUV39H1 in HSC Perturbs Heterochromatin and B Lymphoid Differentiation. *Stem Cell Reports* **6:** 970-984.

Erdel F, Rippe K. 2018. Formation of Chromatin Subcompartments by Phase Separation. *Biophys J* **114:** 2262-2270.

Evertts AG, Manning AL, Wang X, Dyson NJ, Garcia BA, Coller HA. 2013. H4K20 methylation regulates quiescence and chromatin compaction. *Mol Biol Cell* **24:** 3025-3037.

Fabre B, Lambour T, Garrigues L, Ducoux-Petit M, Amalric F, Monsarrat B, Burlet-Schiltz O, Bousquet-Dubouch MP. 2014. Label-free quantitative proteomics reveals the dynamics of proteasome complexes composition and stoichiometry in a wide range of human cell lines. *J Proteome Res* **13:** 3027-3037.

Farras R, Baldin V, Gallach S, Acquaviva C, Bossis G, Jariel-Encontre I, Piechaczyk M. 2008. JunB breakdown in mid-/late G2 is required for down-regulation of cyclin A2 levels and proper mitosis. *Mol Cell Biol* **28:** 4173-4187.

Filipponi D, Muller J, Emelyanov A, Bulavin DV. 2013. Wip1 controls global heterochromatin silencing via ATM/BRCA1-dependent DNA methylation. *Cancer Cell* **24:** 528-541.

Geng F, Tansey WP. 2012. Similar temporal and spatial recruitment of native 19S and 20S proteasome subunits to transcriptionally active chromatin. *Proc Natl Acad Sci U S A* **109:** 6060-6065.

Grewal SI, Jia S. 2007. Heterochromatin revisited. *Nat Rev Genet* **8:** 35-46.

Guillot PV, Xie SQ, Hollinshead M, Pombo A. 2004. Fixation-induced redistribution of hyperphosphorylated RNA polymerase II in the nucleus of human cells. *Exp Cell Res* **295:** 460-468.

Janssen A, Colmenares SU, Karpen GH. 2018. Heterochromatin: Guardian of the Genome. *Annu Rev Cell Dev Biol* **34:** 265-288.

Jegou T, Chung I, Heuvelman G, Wachsmuth M, Gorisch SM, Greulich-Bode KM, Boukamp P, Lichter P, Rippe K. 2009. Dynamics of telomeres and promyelocytic leukemia nuclear bodies in a telomerase-negative human cell line. *Mol Biol Cell* **20:** 2070-2082.

Jonik-Nowak B, Menneteau T, Fesquet D, Baldin V, Bonne-Andrea C, Mechali F, Fabre B, Boisguerin P, de Rossi S, Henriquet C, Pugniere M, Ducoux-Petit M, Burlet-Schiltz O, Lamond AI, Fort P, Boulon S, Bousquet MP, Coux O. 2018. PIP30/FAM192A is a novel regulator of the nuclear proteasome activator PA28gamma. *Proc Natl Acad Sci U S A* **115:** E6477-E6486.

Kito Y, Matsumoto M, Hatano A, Takami T, Oshikawa K, Matsumoto A, Nakayama KI. 2020. Cell cycle-dependent localization of the proteasome to chromatin. *Sci Rep* **10:** 5801.

Klement K, Goodarzi AA. 2014. DNA double strand break responses and chromatin alterations within the aging cell. *Exp Cell Res* **329:** 42-52.

Kowarz E, Loscher D, Marschalek R. 2015. Optimized Sleeping Beauty transposons rapidly generate stable transgenic cell lines. *Biotechnol J* **10:** 647-653.

Lachner M, O'Carroll D, Rea S, Mechtler K, Jenuwein T. 2001. Methylation of histone H3 lysine 9 creates a binding site for HP1 proteins. *Nature* **410:** 116-120.

Larson AG, Elnatan D, Keenen MM, Trnka MJ, Johnston JB, Burlingame AL, Agard DA, Redding S, Narlikar GJ. 2017. Liquid droplet formation by HP1alpha suggests a role for phase separation in heterochromatin. *Nature* **547:** 236-240.

Le Feuvre AY, Dantas-Barbosa C, Baldin V, Coux O. 2009. High yield bacterial expression and purification of active recombinant PA28alphabeta complex. *Protein Expr Purif* **64:** 219-224.

Levy-Barda A, Lerenthal Y, Davis AJ, Chung YM, Essers J, Shao Z, van Vliet N, Chen DJ, Hu MC, Kanaar R, Ziv Y, Shiloh Y. 2011. Involvement of the nuclear proteasome activator PA28gamma in the cellular response to DNA double-strand breaks. *Cell Cycle* **10:** 4300-4310.

Li S, Jiang C, Pan J, Wang X, Jin J, Zhao L, Pan W, Liao G, Cai X, Li X, Xiao J, Jiang J, Wang P. 2015. Regulation of c-Myc protein stability by proteasome activator REGgamma. *Cell Death Differ* **22:** 1000-1011.

Li X, Amazit L, Long W, Lonard DM, Monaco JJ, O'Malley BW. 2007. Ubiquitin- and ATP-independent proteolytic turnover of p21 by the REGgamma-proteasome pathway. *Mol Cell* **26:** 831-842.

Liao T, Wang YJ, Hu JQ, Wang Y, Han LT, Ma B, Shi RL, Qu N, Wei WJ, Guan Q, Xiang J, Chen JY, Sun GH, Li DS, Mu XM, Ji QH. 2018. Histone methyltransferase KMT5A gene modulates oncogenesis and lipid metabolism of papillary thyroid cancer in vitro. *Oncol Rep* **39:** 2185-2192.

Lippman Z, Gendrel AV, Black M, Vaughn MW, Dedhia N, McCombie WR, Lavine K, Mittal V, May B, Kasschau KD, Carrington JC, Doerge RW, Colot V, Martienssen R. 2004. Role of transposable elements in heterochromatin and epigenetic control. *Nature* **430:** 471-476.

Lleres D, James J, Swift S, Norman DG, Lamond AI. 2009. Quantitative analysis of chromatin compaction in living cells using FLIM-FRET. *J Cell Biol* **187:** 481-496.

Luijsterburg MS, Dinant C, Lans H, Stap J, Wiernasz E, Lagerwerf S, Warmerdam DO, Lindh M, Brink MC, Dobrucki JW, Aten JA, Fousteri MI, Jansen G, Dantuma NP, Vermeulen W, Mullenders LH, Houtsmuller AB, Verschure PJ, van Driel R. 2009. Heterochromatin protein 1 is recruited to various types of DNA damage. *J Cell Biol* **185:** 577-586.

Ma CP, Slaughter CA, DeMartino GN. 1992. Identification, purification, and characterization of a protein activator (PA28) of the 20 S proteasome (macropain). *J Biol Chem* **267:** 10515-10523.

Ma CP, Willy PJ, Slaughter CA, DeMartino GN. 1993. PA28, an activator of the 20 S proteasome, is inactivated by proteolytic modification at its carboxyl terminus. *J Biol Chem* **268:** 22514-22519.

Machida S, Takizawa Y, Ishimaru M, Sugita Y, Sekine S, Nakayama JI, Wolf M, Kurumizaka H. 2018. Structural Basis of Heterochromatin Formation by Human HP1. *Mol Cell* **69:** 385-397 e388.

Maison C, Almouzni G. 2004. HP1 and the dynamics of heterochromatin maintenance. *Nat Rev Mol Cell Biol* **5:** 296-304.

Mao I, Liu J, Li X, Luo H. 2008. REGgamma, a proteasome activator and beyond? *Cell Mol Life Sci* **65:** 3971-3980.

Martin C, Zhang Y. 2005. The diverse functions of histone lysine methylation. *Nat Rev Mol Cell Biol* **6:** 838-849.

McCann TS, Tansey WP. 2014. Functions of the proteasome on chromatin. *Biomolecules* **4:** 1026-1044.

Murata S, Kawahara H, Tohma S, Yamamoto K, Kasahara M, Nabeshima Y, Tanaka K, Chiba T. 1999. Growth retardation in mice lacking the proteasome activator PA28gamma. *J Biol Chem* **274:** 38211-38215.

Nielsen PR, Nietlispach D, Mott HR, Callaghan J, Bannister A, Kouzarides T, Murzin AG, Murzina NV, Laue ED. 2002. Structure of the HP1 chromodomain bound to histone H3 methylated at lysine 9. *Nature* **416:** 103-107.

Nishibuchi G, Nakayama J. 2014. Biochemical and structural properties of heterochromatin protein 1: understanding its role in chromatin assembly. *J Biochem* **156:** 11-20.

Oda H, Okamoto I, Murphy N, Chu J, Price SM, Shen MM, Torres-Padilla ME, Heard E, Reinberg D. 2009. Monomethylation of histone H4-lysine 20 is involved in chromosome structure and stability and is essential for mouse development. *Mol Cell Biol* **29:** 2278-2295.

Otterstrom J, Castells-Garcia A, Vicario C, Gomez-Garcia PA, Cosma MP, Lakadamyali M. 2019. Super-resolution microscopy reveals how histone tail acetylation affects DNA compaction within nucleosomes in vivo. *Nucleic Acids Res* **47:** 8470-8484.

Padeken J, Zeller P, Gasser SM. 2015. Repeat DNA in genome organization and stability. *Curr Opin Genet Dev* **31:** 12-19.

Rechsteiner M, Hill CP. 2005. Mobilizing the proteolytic machine: cell biological roles of proteasome activators and inhibitors. *Trends Cell Biol* **15:** 27-33.

Saksouk N, Simboeck E, Dejardin J. 2015. Constitutive heterochromatin formation and transcription in mammals. *Epigenetics Chromatin* **8:** 3.

Sawyer IA, Bartek J, Dundr M. 2019. Phase separated microenvironments inside the cell nucleus are linked to disease and regulate epigenetic state, transcription and RNA processing. *Semin Cell Dev Biol* **90:** 94-103.

Schneider CA, Rasband WS, Eliceiri KW. 2012. NIH Image to ImageJ: 25 years of image analysis. *Nat Methods* **9:** 671-675.

Schotta G, Lachner M, Sarma K, Ebert A, Sengupta R, Reuter G, Reinberg D, Jenuwein T. 2004. A silencing pathway to induce H3-K9 and H4-K20 trimethylation at constitutive heterochromatin. *Genes Dev* **18:** 1251-1262.

Seo HD, Choi Y, Kim M, Kang K, Urano T, Lee D. 2017. The 19S proteasome is directly involved in the regulation of heterochromatin spreading in fission yeast. *J Biol Chem* **292:** 17144-17155.

Shoaib M, Walter D, Gillespie PJ, Izard F, Fahrenkrog B, Lleres D, Lerdrup M, Johansen JV, Hansen K, Julien E, Blow JJ, Sorensen CS. 2018. Histone H4K20 methylation mediated chromatin compaction threshold ensures genome integrity by limiting DNA replication licensing. *Nat Commun* **9:** 3704.

Soderberg O, Gullberg M, Jarvius M, Ridderstrale K, Leuchowius KJ, Jarvius J, Wester K, Hydbring P, Bahram F, Larsson LG, Landegren U. 2006. Direct observation of individual endogenous protein complexes in situ by proximity ligation. *Nat Methods* **3:** 995-1000.

Strom AR, Emelyanov AV, Mir M, Fyodorov DV, Darzacq X, Karpen GH. 2017. Phase separation drives heterochromatin domain formation. *Nature* **547:** 241-245.

Sun L, Fan G, Shan P, Qiu X, Dong S, Liao L, Yu C, Wang T, Gu X, Li Q, Song X, Cao L, Li X, Cui Y, Zhang S, Wang C. 2016. Regulation of energy homeostasis by the ubiquitin-independent REGgamma proteasome. *Nat Commun* **7:** 12497.

Tardat M, Murr R, Herceg Z, Sardet C, Julien E. 2007. PR-Set7-dependent lysine methylation ensures genome replication and stability through S phase. *J Cell Biol* **179:** 1413-1426.

Thiru A, Nietlispach D, Mott HR, Okuwaki M, Lyon D, Nielsen PR, Hirshberg M, Verreault A, Murzina NV, Laue ED. 2004. Structural basis of HP1/PXVXL motif peptide interactions and HP1 localisation to heterochromatin. *Embo J* **23:** 489-499.

Trembecka-Lucas DO, Szczurek AT, Dobrucki JW. 2013. Dynamics of the HP1beta-PCNA-containing complexes in DNA replication and repair. *Nucleus* **4:** 74-82.

Ustrell V, Hoffman L, Pratt G, Rechsteiner M. 2002. PA200, a nuclear proteasome activator involved in DNA repair. *Embo J* **21:** 3516-3525.

van Dijk J, Bompard G, Cau J, Kunishima S, Rabeharivelo G, Mateos-Langerak J, Cazevieille C, Cavelier P, Boizet-Bonhoure B, Delsert C, Morin N. 2018. Microtubule polyglutamylation and acetylation drive microtubule dynamics critical for platelet formation. *BMC Biol* **16:** 116.

Verschure PJ, van der Kraan I, de Leeuw W, van der Vlag J, Carpenter AE, Belmont AS, van Driel R. 2005. In vivo HP1 targeting causes large-scale chromatin condensation and enhanced histone lysine methylation. *Mol Cell Biol* **25:** 4552-4564.

Welk V, Coux O, Kleene V, Abeza C, Trumbach D, Eickelberg O, Meiners S. 2016. Inhibition of Proteasome Activity Induces Formation of Alternative Proteasome Complexes. *J Biol Chem* **291:** 13147-13159.

Wilk S, Chen WE, Magnusson RP. 2000. Properties of the nuclear proteasome activator PA28gamma (REGgamma). *Arch Biochem Biophys* **383:** 265-271.

Zannini L, Buscemi G, Fontanella E, Lisanti S, Delia D. 2009. REGgamma/PA28gamma proteasome activator interacts with PML and Chk2 and affects PML nuclear bodies number. *Cell Cycle* **8:** 2399-2407.

Zannini L, Lecis D, Buscemi G, Carlessi L, Gasparini P, Fontanella E, Lisanti S, Barton L, Delia D. 2008. REGgamma proteasome activator is involved in the maintenance of chromosomal stability. *Cell Cycle* **7:** 504-512.

Figure legends

Figure 1. PA28γ and HP1β co-localize in α4-GFP-20S proteasome foci.

A. Stable asynchronously growing U2OS (Tet-Off) α4-GFP cells were induced for the expression of GFP-tagged α4 subunit of the 20S proteasome (α4-GFP, green) for 24 hours in the absence of tetracycline, then fixed and stained with DAPI (blue). Scale bar, 10 μm.

B. Induced U2OS-α4-GFP cells (α4-GFP, green), as in A, were immunostained with antibody raised against alpha 6 subunit of the 20S proteasome (α6, left panel), the regulatory complex PA28γ (PA28γ, middle panel) and a subunit of the 19S regulatory complex (Rpt6, right panel), all in grey. Scale bar, 10 μm.

C. α4-GFP foci are associated with chromatin. Induced U2OS-α4-GFP cells (α4-GFP, green), as in A, were not treated (- CSK buffer) or treated (+ CSK buffer) with an extraction CSK buffer, then fixed and immunostained with anti-PA28γ antibodies (red). Scale bar, 5 μm.

D. Induced U2OS-α4-GFP cells (α4-GFP, green) were immunostained with anti-HP1β antibodies (grey). A merge image of GFP and HP1β signal is shown. Scale bar, 10 μm. Arrows indicate sites of co-localization between HP1β and α4-GFP.

E. Co-immunoprecipitation of PA28γ and HP1β in asynchronous induced U2OS-α4-GFP cells. Induced U2OS-α4-GFP cells, as in A, were lysed and subjected to pull-down with either an antibody raised against PA28γ or GFP-TRAP, or the appropriate isotype control (CTL). An immunoblot of the pull-down (IP) and supernatant (SN) from whole-cell extracts (WCE) was probed with the antibodies indicated.

F. U2OS-α4-GFP cells were transfected with si-Luc, si-PA28γ or si-HP1β. One day later, the expression of α4-GFP was induced, and cells were recovered 48 hours after siRNA treatment. Immunostaining was performed to detect PA28γ (red) and HP1β (magenta) in cells treated with the siRNA indicated. Representative images are shown (left). Arrows indicate cells with α4-GFP and PA28γ foci. Scale bar, 10 μm. The percentage of cells with α4-GFP foci is shown in the bar graph (right). Error bars derived from 3 independent experiments represent the mean ± SD, $n \geq 47$ cells per condition. One-way ANOVA analysis, $p = 0.0001$ (****) for siRNA-PA28γ and -HP1β versus WT.

Figure 2. Endogenous HP1β, PA28 and the 20S proteasome co-localize in U2OS cells.

A. Nuclear localization of endogenous HP1β (left panel) and PA28γ (middle panel) by immunofluorescence in asynchronous U2OS cells after pre-permeabilization with 0.5% Triton

X-100. A representative merged image of HP1β (green) and PA28γ (red), and higher-magnification views are shown (right panel). Scale bars, 10 μm.

B. A representative Airyscan confocal Z-projected image showing the co-detection of HP1β (green) and PA28γ (red) (left). Co-localizations of both proteins along the cross is shown. Scale bars, 5 μm. Using the co-localization module of Imaris, a representative image of HP1β (green), PA28γ (red) and co-localization spots (white/grey) corresponding to 3-D image (middle panel) is shown with the corresponding image showing only co-localization spots (right panel). Scale bars, 5 μm.

C. Immunoblot analysis of PA28γ expression level in total extracts of U2OS cells treated or not with si-PA28γ, used for *in situ* Proximity Ligation Assay (*is*-PLA) (left panel). Tubulin was used as a loading control. The relative abundance of PA28γ was quantified using ImageJ software. Control (CTL) or si-PA28γ treated U2OS cells were subjected to *is*-PLA using primary antibodies directed against HP1β and PA28γ, and DNA stained with DAPI. Positive PLA signals appear as green dots and higher magnification views of a nucleus are shown (middle panel). Scale bars, 10 μm. Quantification of PLA dots was carried out using an ImageJ plugin (see Materials and Methods). The number of PLA dots per nucleus for HP1β/PA28γ interaction in control (CTL) or si-PA28γ treated cells is shown graphically (right panel). Data represent the means ± SD from 3 independent experiments, the number of analyzed cells is $n = 78$ and $n = 45$ in control and si-PA28γ treated cells, respectively. The *p*-value was determined with Student's T-test, **** ($p = 0.0001$).

D. Immunoblot analysis of HP1β expression level in total extracts from U2OS cells treated or not with si-HP1β (upper left panel). Tubulin was used as a loading control. The relative abundance of HP1β proteins was quantified using ImageJ software. Control (CTL) or si-HP1β treated U2OS cells were subjected to *is*-PLA using primary antibodies directed against HP1β and α4 (a subunit of the 20S proteasome), and DNA was stained with DAPI. Positive PLA signals appear as green dots. A higher magnification view of a nucleus is shown (lower left panel). Scale bar, 10 μm. The number of PLA dots per nucleus for HP1β/α4 interaction in control (CTL) or si-HP1β treated cells is shown on the bar graph (right panel). Data represent the means ± SD from 3 independent experiments, the number of cells analyzed is $n = 48$ and $n = 46$ in control cells and si-HP1β treated cells, respectively. *p*-value was determined with Student's T-test, ****($p < 0.0001$).

Figure 3. PA28γ is present on heterochromatin and its depletion induces a decompaction of pericentromeric heterochromatin.

A. ChIP-qPCR analysis of PA28γ levels at different repetitive elements located in heterochromatin or euchromatin (as indicated on the x-axis) in wild type (WT) *versus* KO-PA28γ U2OS cells (right panel). Data are represented as relative enrichment of PA28γ antibody *versus* H3 control as shown on the y-axis. Data are means ± SEM (n = 5). Significance was calculated by Student's T-test, $^{**}p < 0.01$ (p = 0.0046, L1 LINE), $^{***}p < 0.001$ (p = 0.00011, Sat II), $^{****}p < 0.0001$ (p = 2.09E-05, p = 5.15E-05 and p = 2,54318E-06), HERV-K, α-Sat and CCNE2 respectively).

B. U2OS-LacO cells, treated or not with si-HP1β or si-Luc, were transiently transfected with GFP-LacI construct the same day and were recovered 48 hours later. Proteins were analyzed by immunoblotting. The relative abundance of HP1β in the extracts was quantified using ImageJ software and normalized to tubulin (upper panel). Cells on coverslips were immunostained with anti- HP1β (red) and the GFP signal was imaged in parallel (green). DNA was stained with DAPI (cyan). Representative fluorescence and immunofluorescence images of Z-stack projections of U2OS-LacO cells are shown. Magnified views of GFP-LacI spot are shown in inserts. Scale bars, 10 μm.

C. Quantitative analysis of the decompaction of the LacO array. Z-stacks images were acquired on U2OS-LacO cells treated as in (B) and the area of the GFP-LacI signal was quantified on a Z-projection using the ImageJ software (see Materials and Methods). Data represent the means ± SD from three biological repeats, numbers of analyzed nuclei with GFP-LacI spot were n = 30, n = 28 and n = 27 in control cells (CTL), si-HP1β or si-Luc treated cells, respectively. (ns, no significant p = 0.2503, *** p = 0.0003; $^{**}p$ = 0.001, p-values were determined by a 2-way ANOVA test).

D. U2OS-LacO cells, treated or not with a si-PA28γ or si-Luc, were transiently transfected with GFP-LacI construct the same day, recovered 48 hours later and cells were analyzed as in B. Immunostaining was performed against PA28γ (red). Representative fluorescence and immunofluorescence images of Z-stack projections of U2OS-LacO cells are shown. Magnified views of the GFP-LacI spot are shown in inserts. Scale bars, 10 μm.

E. Quantitative analysis of the decompaction of the LacO array. Z-stack images were acquired on U2OS-LacO cells treated as in D and the area of the GFP-LacI signal was quantified as in C. Data represent the means ± SD from three biological repeats, numbers of

analyzed nuclei with GFP-LacI spot were $n = 30$, $n = 31$ and $n = 29$ in control cells (CTL), si-PA28γ or si-Luc treated cells, respectively. (ns, not significant *** $p = 0.0002$; ** $p = 0.0013$, values were determined by Tukey's multiple comparisons test.

Figure 4. PA28γ controls chromatin compaction, independently of its interaction with the 20S proteasome.

A. Immunoblot analysis of PA28γ expression level in total extracts from parental (WT) and PA28γ-knockout (KO-PA28γ) HeLa$^{H2B\text{-}2FPs}$ cells. Tubulin was used as a loading control.

B. FRET analysis in asynchronous parental (WT) and PA28γ-knockout (KO-PA28γ) HeLa$^{H2B\text{-}FPs}$ cells. FLIM-FRET measurements were performed and the spatial distribution of the FRET efficiency is represented in a continuous pseudo-color scale ranging from 0 to 30 % (left panel). Scale bars, 10 μm. Right panel, statistical analysis of the mean FRET efficiency percentage in WT and KO-PA28γ HeLa$^{H2B\text{-}2FPs}$ nuclei, presented as box-and-whisker plots. The thick line represents median, the boxes correspond to the mean FRET values upper and lower of the median, with the whiskers covering the 10-90 percentile range. Data represent the means ± SD from 4-6 independent experiments, the total number of analyzed cells is n = 154 nuclei (WT) and n = 132 nuclei (KO-PA28γ), **** $p < 0.0001$ (Student's T-test).

C. Spatial distribution of the FRET efficiency (percentage) in representative WT and KO-PA28γ HeLa$^{H2B\text{-}2FPs}$ nuclei. The FRET percentage distribution is depicted in a continuous pseudo-color scale ranging from 0 to 30% (left panel). Scale bars, 10 μm. FRET distribution graph shows distinct populations of FRET efficiency in WT and KO-PA28γ cells (blue and black curves, respectively) (right panel).

D. Spatial distribution of the FRET efficiency (percentage) in representative WT, KO-PA28γ and KO/KI-WT #6, KO/KI-WT #8 HeLa$^{H2B\text{-}2FPs}$ nuclei. The FRET percentage distribution is depicted as in C. Scale bars, 10 μm. Quantification of the mean FRET efficiency was represented as box-and-whisker plots. Data represent the means ± SD from 3 independent experiments, the total number of analyzed cells is n = 102 nuclei (WT), n = 90 (KO-PA28γ), n = 53 (KO/KI-WT #6), n = 54 (KO/KI-WT #8). n.s not significant, **** p <0.0001 (Student's T-test).

E. Cell extracts from parental HeLa$^{H2B\text{-}FPs}$ (WT), PA28γ-knockout (KO-PA28γ) cells and KO cells re-expressing the wild-type form (KO/KI-WT) or the ΔC-mutant (KO/KI-ΔC) of PA28γ, treated for 2 hours with 25 μM of MG132, were subjected to immunoprecipitation using anti-

PA28γ antibodies. Immunoblots of the supernatant (SN-IP) and the pull-down (IP- PA28γ) from whole cell extracts were probed with the antibodies indicated.

F. Spatial distribution of the FRET efficiency (percentage) in representative WT, KO-PA28γ and KO cells re-expressing the ΔC-mutant (KO/KI-ΔC) HeLa$^{H2B\text{-}2FPs}$ nuclei. The FRET percentage distribution is depicted as in B (left panel). Scale bars, 10 μm. Quantification of the FLIM-FRET measurements. Data represent the means ± SD from 3 independent experiments, the total number of analyzed cells is n = 102 nuclei (WT), n = 90 nuclei (KO-PA28γ), n = 83 nuclei (KO/KI-ΔC). n.s, not significant, **** $p < 0.0001$, (Student's T-test).

Figure 5. PA28γ is a crucial factor for chromatin compaction.

A. HeLa$^{H2B\text{-}2FPs}$ cells (WT) were transfected with control si-Luc, si-PA28γ, si-HP1β or a mix of both siRNAs (si-PA28γ/HP1β) for 48 hours. Immunoblot analysis of PA28γ and HP1β protein levels in HeLa^{2FPs} following siRNA treatments were performed. Tubulin and anti-β actin antibodies were used as loading controls. The relative abundance of PA28γ and HP1β proteins was quantified using ImageJ software.

B. Quantification of the mean FRET efficiencies were presented as box-and-whisker plots where the thick line represents median, the boxes correspond to the mean FRET values upper and lower of the median, with the whiskers covering the 10-90 percentile range. Data represent the means ± SD from 4 independent experiments, the total number of analyzed cells is n = 152 (si-Luc), n = 85 (si-PA28γ), n = 73 (si-HP1β), n = 61 (si-PA28γ/HP1β). ns = not significant, *** $p < 0.001$, **** $p < 0.0001$ (Student's T-test).

C. Representative images of the spatial distribution of the FRET efficiency (percentage) in representative control si-Luc, si-PA28γ, si-HP1β, or both siRNAs (si-PA28γ/HP1β) treated HeLa$^{H2B\text{-}2FPs}$ nuclei. Scale bars, 10 μm. Mean FRET distribution graph showing distinct populations of FRET efficiency in si-Luc (blue curve), si-PA28γ (black), si-HP1β (red), or both si-PA28γ/HP1β (green) treated HeLa$^{H2B\text{-}2FPs}$ (right panel).

Figure 6. PA28γ contributes to the maintenance of heterochromatin marks.

A. Representative immunoblots of whole cell extracts from U2OS (WT and KO-PA28γ) cells, using anti-H3K9me3 antibodies. Histone H3 was used as loading control. Graphical representation of the relative abundance of the tri-methylation (H3K9me3) mark on histone H3 normalized to histone H3. The mean ± SD is from four independent experiments. The p-value was determined with a Student's T-test, ns = not significant ($p = 0.9354$).

B. Immunoblots of whole cell extracts from U2OS (WT and KO-PA28γ) cells, using anti-H4K20me3 and anti-H4K20me1 antibodies. Histone H3 was used as loading control. Graphical representation of the relative abundance of the mono-methylation (H4K20me1) and the tri-methylation (H4K20me3) marks on histone H4 normalized to histone H3. The mean ± SD is from four independent experiments. The *p*-value was determined with a Student's T-test, **** ($p \leq 0.0001$).

C and D. ChIP-qPCR analysis of H3K9me3 and H4K20me3 levels in WT *versus* KO-PA28γ U2OS cells. Data are represented as relative enrichment of each specific antibody *versus* H3 control as shown on the y-axis. Data are means ± SEM ($n = 5$ for H3K9me3 and H3, $n = 3$ for H4K20me3). Significance was calculated by Student's T-test, $^{**}p < 0.01$, $^{***}p < 0.001$, $^{****}p < 0.0001$. *p*-values are presented in Table 1.

E. Schematic summary of findings. Upon certain physiological events, decompaction of the chromatin is required and involves a change in H3K9me3 and H4K20me1/3. After this event, chromatin and heterechromatin need to be recompacted. Our results show that in the absence of PA28γ, H3K9me3 and H4K20me3 are reduced and chromatin retains a decompacted form.

SUPPLEMENTARY DATA

Supplementary Methods

Proteasome Activity Assay

Proteasome peptidase activity was measured using black flat-bottom 96-well plates (Nunc) by incubating beads of immunopurified proteasome in 50 µl of activity buffer (20 mM Tris-HCl, pH 7.5, 5 mM $MgCl_2$, 1 mM ATP, 1 mM DTT, 10% Glycerol) containing 100 µM suc-LLVY-AMC, in the presence or absence of 25 µM MG132 (Enzo Life Science), for 20 min at 37°C. Proteasome activity was determined by the detection of the free AMC fluorescence using a FLx800 microplate fluorescence reader (excitation 380 nm, emission 440 nm, Bio-Tek Instruments).

Figure Supplementary

Figure S1. α4-GFP is incorporated into active proteasome and α4-GFP foci fluctuate during the cell cycle.

A. GFP-pull-downs from U2OS and U2OS-α4-GFP cell lysates were subjected to proteasome activity measurements using an exogenous peptide (suc-LLVY-AMC) in the absence or the presence of an inhibitor of the 20S proteasome activity (MG132, 25 μM).

B. U2OS cells, transfected (right panel) or not (left panel) with a vector allowing the expression of α4 without any tag protein. After 24 hours, both cell lines were immunostained with anti-alpha 4 antibodies. Representative images are shown. Scale bars, 10 μm. Arrows indicate α4 foci.

C. Asynchronous induced U2OS-α4-GFP cells (AS) were synchronized at the G1/S phase boundary by hydroxyurea treatment (10 mM, 16 hours) (HU) then released from HU-block for 4, 6, 8 10 and 11 hours (R4h, R6h, R8h, R10h and R11h, respectively). Cells were subjected to GFP microscopy detection and flow cytometry analysis. Upper panel: bar graph indicates the percentage of cells with nuclear α4-GFP foci observed by fluorescence microscopy. Error bars derived from 3 independent experiments represent the mean ± SD. (ns = no significant, ** $p < 0.001$; *$p < 0.5$, p-values were determined by One-way ANOVA test and are presented in Table 2. Lower panel: bar graph representing the percentage of cells in G1, S and G2/M phases of the cell cycle, obtained by FACS analysis.

Figure S2. Co-localization of PA28γ with HP1α and HP1β/PA28γ co-localization is independent of PIP30, a regulator of PA28γ.

A. Immunoblot of whole cell extract (30 μg) from asynchronous parental (WT) and KO-PA28γ (KO-PA28γ) U2OS cells, using anti-PA28γ. Tubulin was used as a loading control (left panel). Asynchronously-growing U2OS-KO-PA28γ cells were pre-permeabilized with 0.5 % Triton-X100 before fixation and the detection of endogenous HP1β (left panel) and PA28γ (middle panel) by indirect immunofluorescence using anti-HP1β and PA28γ antibodies. A representative merged image of HP1β (green) and PA28γ (red) is shown (right panel). Scale bars, 10 μm.

B. *In situ* Proximity ligation assay (*is*-PLA) was carried out in asynchronous U2OS cell line. Fixed cells were treated with primary antibodies directed against PA28γ (mouse monoclonal) and HP1α (rabbit polyclonal) (CTL) or with only PA28γ antibodies (w/o anti-HP1α) and DNA was stained with DAPI (left panel). A higher magnification view of a nucleus is shown. Scale bars, 10 μm. The number of PLA dots per nucleus in cells treated with both antibodies (CTL) or with only PA28γ antibodies (w/o anti-HP1α) is shown on the bar graph (right panel). Data represent the mean ± SD from 3 independent experiments, the number of cells

analyzed was n = 40 and n = 41 in control cells and cells treated without primary HP1α antibody, respectively. The p-value was determined with Student's T-test, **** ($p \leq 0.0001$).

C. Whole-cell extracts (30 μg) of parental (WT), PA28γ-knockout (KO-PA28γ) and PIP30-knock-out (KO-PIP30) U2OS cells used for the *is*-PLA were analyzed by SDS-PAGE and immunoblotted with the antibodies indicated (left panel). *Is*-PLA was carried out using primary antibodies directed against HP1β and PA28γ, and DNA was stained with DAPI. Representative images of parental (WT) and KO-PIP30 U2OS cells are presented and higher magnification views are shown (middle panel). Scale bars, 10 μm. Quantification of PLA-dots was performed as in Fig 2C. The number of PLA-dots per nucleus is shown on the bar graph (right panel). Data represent the mean ± SD from 3 independent experiments; the number of cells analyzed was n= 59 (WT), n = 40 (KO-PIP30) and n = 42 (KO-PA28γ). Statistical significance was evaluated based on one-way ANOVA analysis (ns = not significant, and *** $p < 0.0001$ were obtained for KO-PIP30 and KO-PA28γ versus WT).

Figure S3. HP1β is present at the same repetitive elements than PA28γ.

Immunoblot analysis of HP1β expression level in total extracts from U2OS cells treated or not with si-HP1β (left panel). Tubulin was used as a loading control. The relative abundance of HP1β proteins was quantified using ImageJ software. ChIP-qPCR analysis of HP1β levels at different repetitive elements (as indicated on the x-axis) in U2OS cells treated with si-Luc or si-HP1β. Data are represented as relative enrichment of HP1β antibody *versus* H3 control as shown on the y-axis (right panel). Data are means +/- SEM (n = 5). Significance was calculated with Student's T-test, ns = not significant $p \geq 0.05$, ** $p < 0.01$ and *** $p < 0.001$. p-values are presented in Table 3.

Figure S4. Endogenous PA28γ and HP1β co-localize in HeLa cells.

Immunoblot analysis of PA28γ expression level in total extracts from HeLa cells, treated or not with si-PA28γ (left panel). Tubulin was used as loading control (left panel). The relative abundance of PA28γ proteins was quantified using ImageJ software. Control (CTL) or si-PA28γ (si- PA28γ) treated HeLa cells were subjected to *is*-PLA using primary antibodies directed against HP1β and PA28γ, and DNA was stained with DAPI. Positive PLA signals appear as green dots, and a higher magnification view of a nucleus is shown (middle panel). Scale bars, 10 μm. Quantification of PLA dots was carried out using an ImageJ plugin (see Materials and Methods). The number of PLA dots per nucleus for HP1β/PA28γ interaction in

control (CTL) or si-PA28γ treated cells is shown graphically (right panel). Data represent the means ± SD from 3 independent experiments, the number of analyzed cells is $n = 40$ and $n = 34$ in control and si-PA28γ treated cells, respectively. p value was determined with Student's T-test, ** $p = 0.0016$.

Figure S5. PA28γ-depletion does not alter the expression level of H2B-GFP or mCherry-H2B, and analysis of re-expression of WT- and ΔC- PA28γ in HeLa$^{H2B\text{-}2FPs}$ cells.

A. Immunoblot analysis of H2B-GFP and mCherry-H2B expression level in total extracts from parental (WT) and KO-PA28γ HeLa$^{H2B\text{-}2FPs}$ cells (left panel). Tubulin was used as a loading control. The relative abundance of HP1β proteins was quantified using ImageJ software. Graphical representation of the relative abundance of H2B-GFP and mCherry-H2B normalized to tubulin (right panel). The mean ± SD is from four independent experiments. Statistical significance was evaluated based on Student's T-test, ns = not significant. (p = 0.2027 and 0.4024 for H2B-GFP and mCherry-H2B, respectively)

B. Quantification of the H2B-GFP and mCherry-H2B fluorescence intensities in WT and KO-PA28γ HeLa$^{H2B\text{-}2FPs}$ cells. The total number of analyzed cells is $n = 172$ (WT), $n = 183$ (KO-PA28γ). Statistical significance was evaluated with Student's T-test, ns= not significant.

C. FRET analysis in WT, KO-PA28γ HeLa$^{H2B\text{-}FPs}$ cells, and WT HeLa$^{H2B\text{-}FPs}$ cells treated with Trichostatin A (TSA, 200ng/ml, 24h). The statistical analysis of the mean FRET efficiency percentage is presented as box-and-whisker plots. The thick line represents median, the boxes correspond to the mean FRET values upper and lower of the median, with the whiskers covering the 10-90 percentile range. The total number of analyzed nuclei is $n = 154$ (WT), $n = 132$ (KO-PA28γ), and $n = 33$ (WT + TSA), **** $p < 0.0001$ (Student's T-test).

D. Immunoblot analysis of PA28γ expression level in total extracts from parental (WT), PA28γ-knockout (KO-PA28γ) HeLa$^{H2B\text{-}2FPs}$ cells and two independent clones of HeLa$^{H2B\text{-}2FPs}$ cells knocked out for PA28γ in which wild-type PA28γ was stably re-expressed (KO/KI-WT #6, KO/KI-WT #8). Tubulin was used as a loading control.

E. Whole-cell extracts from parental HeLa$^{H2B\text{-}2FPs}$ (WT), PA28γ-knockout (KO-PA28γ) cells and KO cells re-expressing the wild-type (KO/KI-WT#8) form or the ΔC-mutant (KO/KI-ΔC) of PA28γ. Cells were treated or not for 2 hours with MG132 (25 μM), and whole cell extracts analyzed by immunoblot using the antibodies indicated.

F. Co-immunoprecipitation of PA28γ and the 20S proteasome from whole-cell extracts without MG132 treatment was analyzed by immunoblotting of the pull-down (IP- PA28γ) and the supernatant (SN-IP 1/10eme) with the antibodies indicated.

Figure S6. PA28γ depletion decreases the S phase duration.

A. Asynchronous parental (WT) and KO-PA28γ U2OS cells were fixed and stained with propidium iodide and then subjected to flow cytometry analysis. The histogram presents the repartition of the cells in the G1, S, and G2/M phases of the cell cycle. Data represent the means ± SD from four independent biological repeats. *p*-values were determined by 2-way ANOVA test, ns = not significant ($p = 0.2407$), *$p < 0.05$ ($p = 0.0312$) and ***$p < 0.001$ ($p = 0.0006$).

B. Asynchronous parental U2OS and U2OS-KO-PA28γ cells, synchronized at the G1/S phase transition by a double thymidine block, then were released for the times indicated and subjected to FACS analysis. Histograms representing the percentage of the cells in S (left panel) and G2/M (right panel) phases of the cell cycle are shown. Data represent the means ± SD from three biological repeats. *p* values were determined with a 2-way ANOVA for each time point. *p*-values are presented in Table 4.

C. Total cell extracts of WT- or -KO-PA28γ U2OS cells, asynchronous (AS) and synchronized at the G1/S phase transition by a double thymidine block and then release procedure were analyzed by immunoblot using the antibodies indicated. β-actin was used as a loading control.

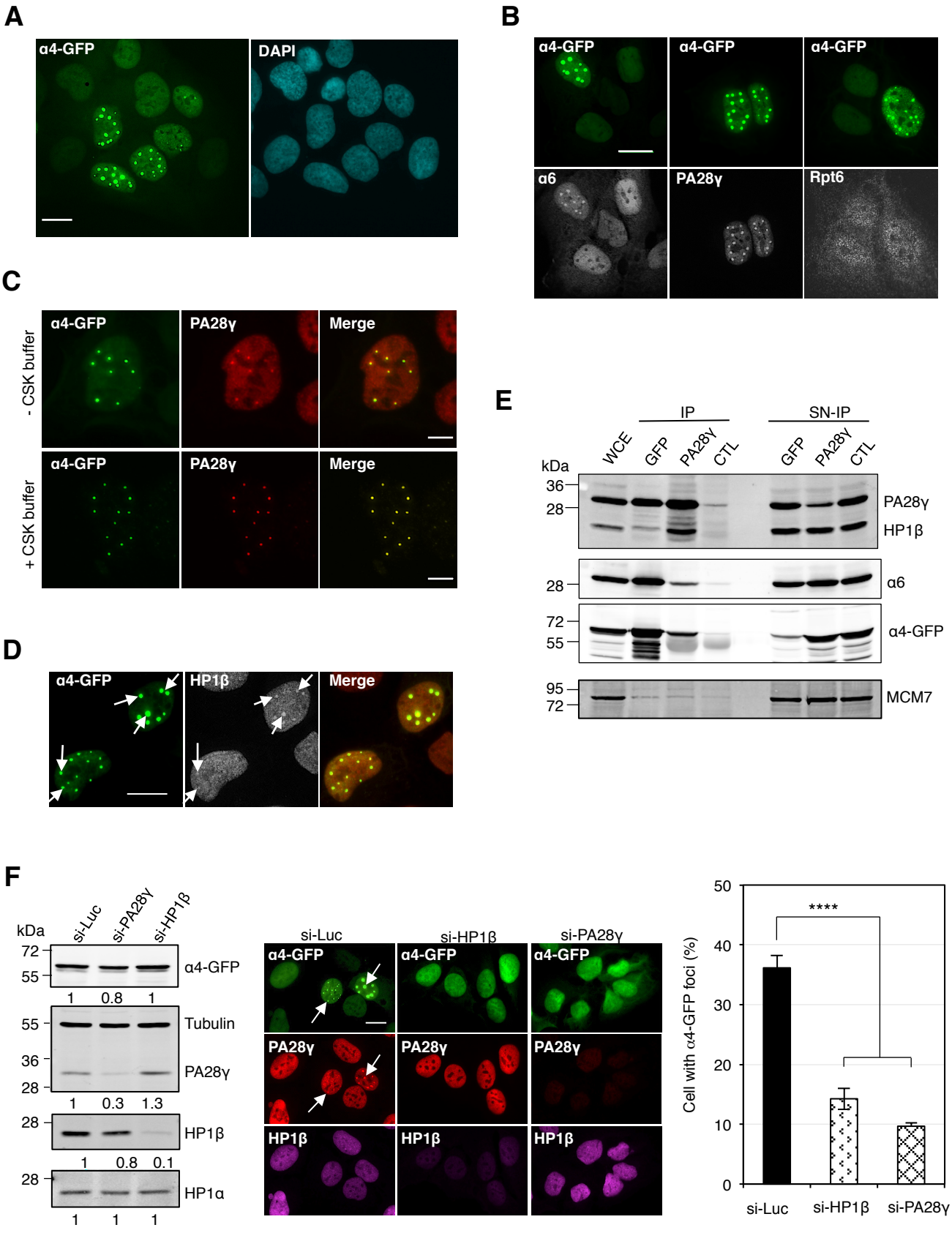
A
α4-GFP
DAPI
B
α4-GFP
α4-GFP
α4-GFP
α6
PA28γ
Rpt6
C
- CSK buffer
+ CSK buffer
α4-GFP
PA28γ
Merge
α4-GFP
PA28γ
Merge
D
α4-GFP
HP1β
Merge
E
IP
SN-IP
kDa
WCE
GFP
PA28γ
CTL
GFP
PA28γ
CTL
36
28
PA28γ
HP1β
28
α6
72
55
α4-GFP
95
72
MCM7
F
kDa
si-Luc
si-PA28γ
si-HP1β
72
55
α4-GFP
1
0.8
1
55
Tubulin
36
28
PA28γ
1
0.3
1.3
28
HP1β
1
0.8
0.1
28
HP1α
1
1
1
si-Luc
si-HP1β
si-PA28γ
α4-GFP
α4-GFP
α4-GFP
PA28γ
PA28γ
PA28γ
HP1β
HP1β
HP1β
Cell with α4-GFP foci (%)
50
40
30
20
10
0
****
si-Luc
si-HP1β
si-PA28γ

Figure 1

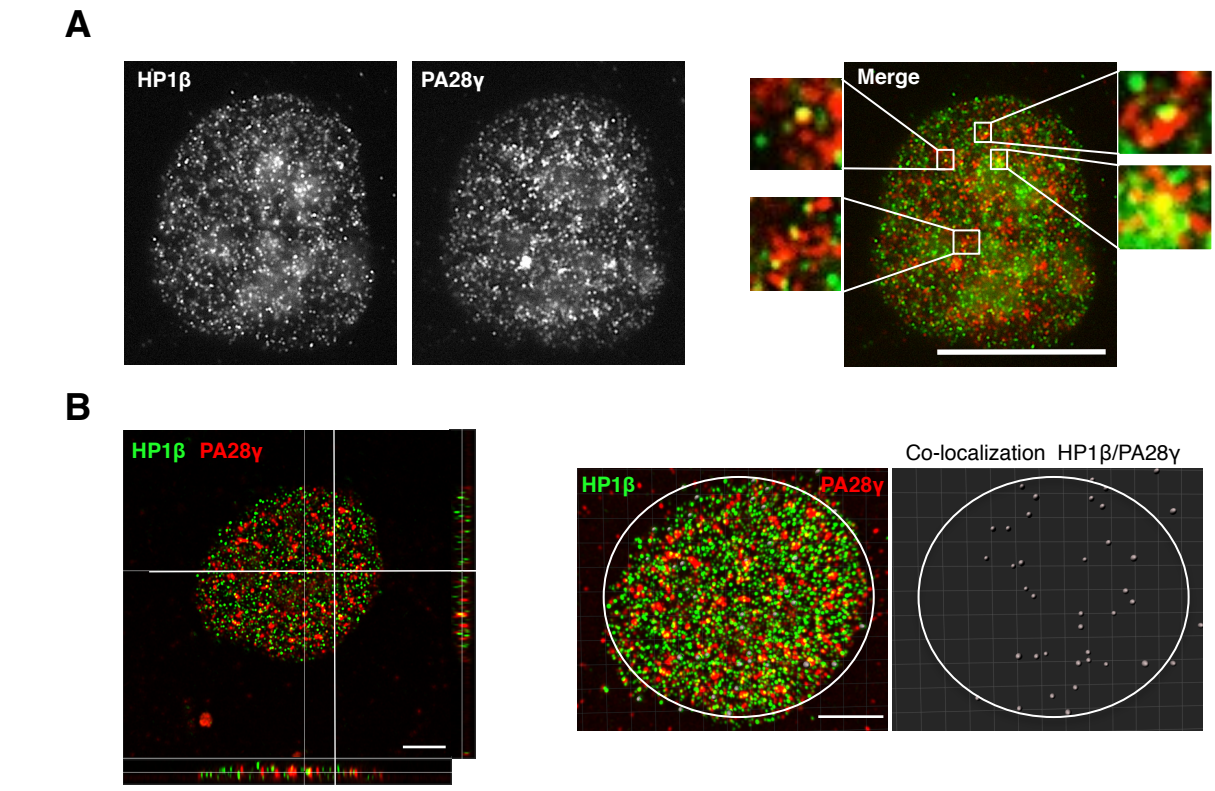
A
HP1β
PA28γ
Merge
B
HP1β PA28γ
Co-localization HP1β/PA28γ
HP1β
PA28γ
C
kDa
CTL
si-PA28γ
36
28
PA28γ
1
0.3
72
55
Tubulin
PLA : PA28γ/HP1β
PLA/ DAPI
CTL
si-PA28γ
PA28γ /HP1β
Number of PLA dots/ nucleus
50
40
30
20
10
0
****
CTL
si-PA28γ
D
kDa
CTL
si-HP1β
28
HP1β
1
0.2
72
55
Tubulin
PLA : α4/HP1β
PLA + DAPI
CTL
si-HP1β
α4 / HP1β
Number of PLA dots/nucleus
60
50
40
30
20
10
0
****
CTL
si-HP1β

Figure 2

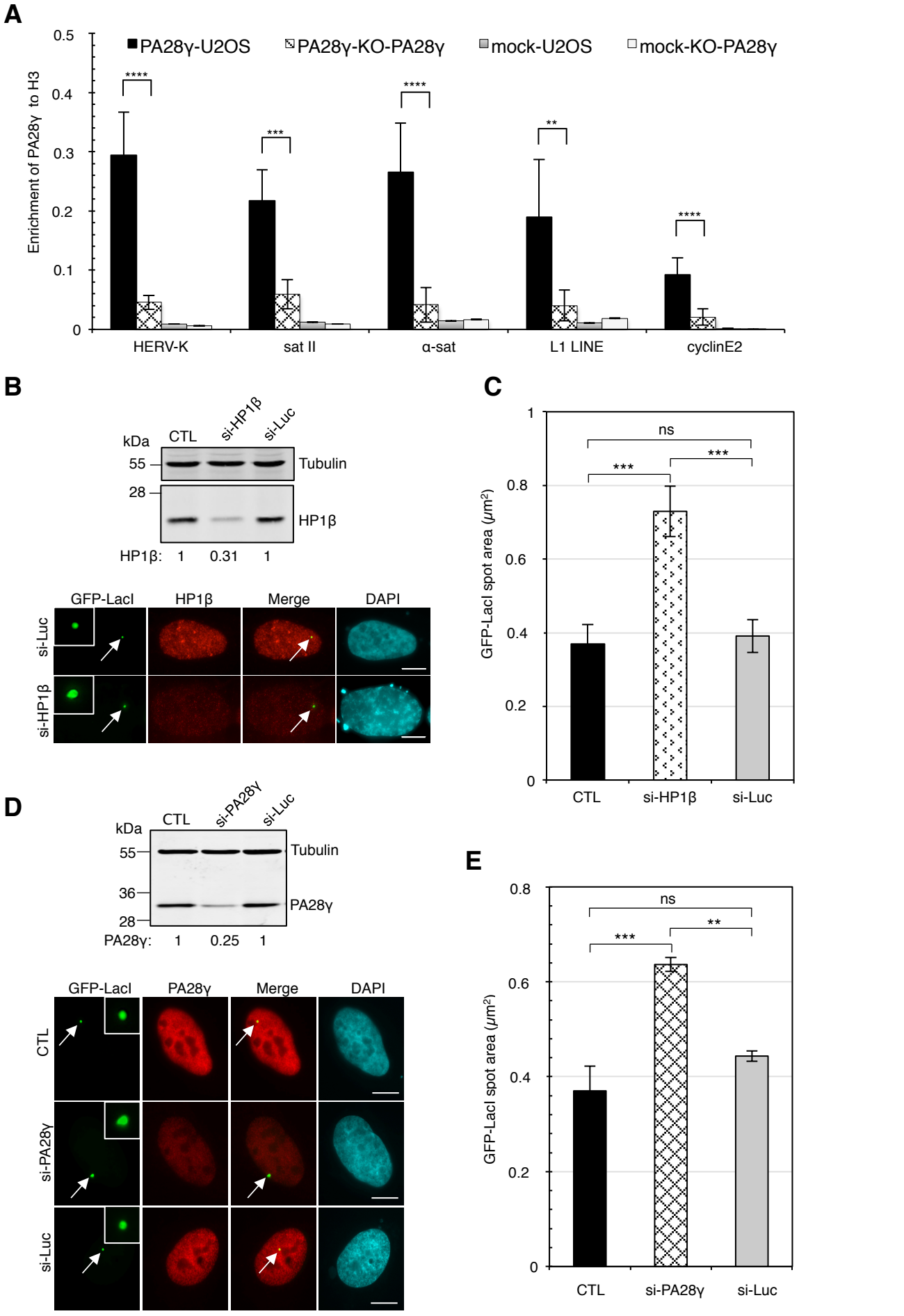
A
PA28γ-U2OS
PA28γ-KO-PA28γ
mock-U2OS
mock-KO-PA28γ
Enrichment of PA28γ to H3
HERV-K
sat II
α-sat
L1 LINE
cyclinE2
B
kDa
CTL
si-HP1β
si-Luc
55
Tubulin
28
HP1β
HP1β: 1 0.31 1
GFP-LacI
HP1β
Merge
DAPI
si-Luc
si-HP1β
C
GFP-LacI spot area (μm²)
ns
CTL
si-HP1β
si-Luc
D
kDa
CTL
si-PA28γ
si-Luc
55
Tubulin
36
PA28γ
28
PA28γ: 1 0.25 1
GFP-LacI
PA28γ
Merge
DAPI
CTL
si-PA28γ
si-Luc
E
GFP-LacI spot area (μm²)
ns
CTL
si-PA28γ
si-Luc

Figure 3

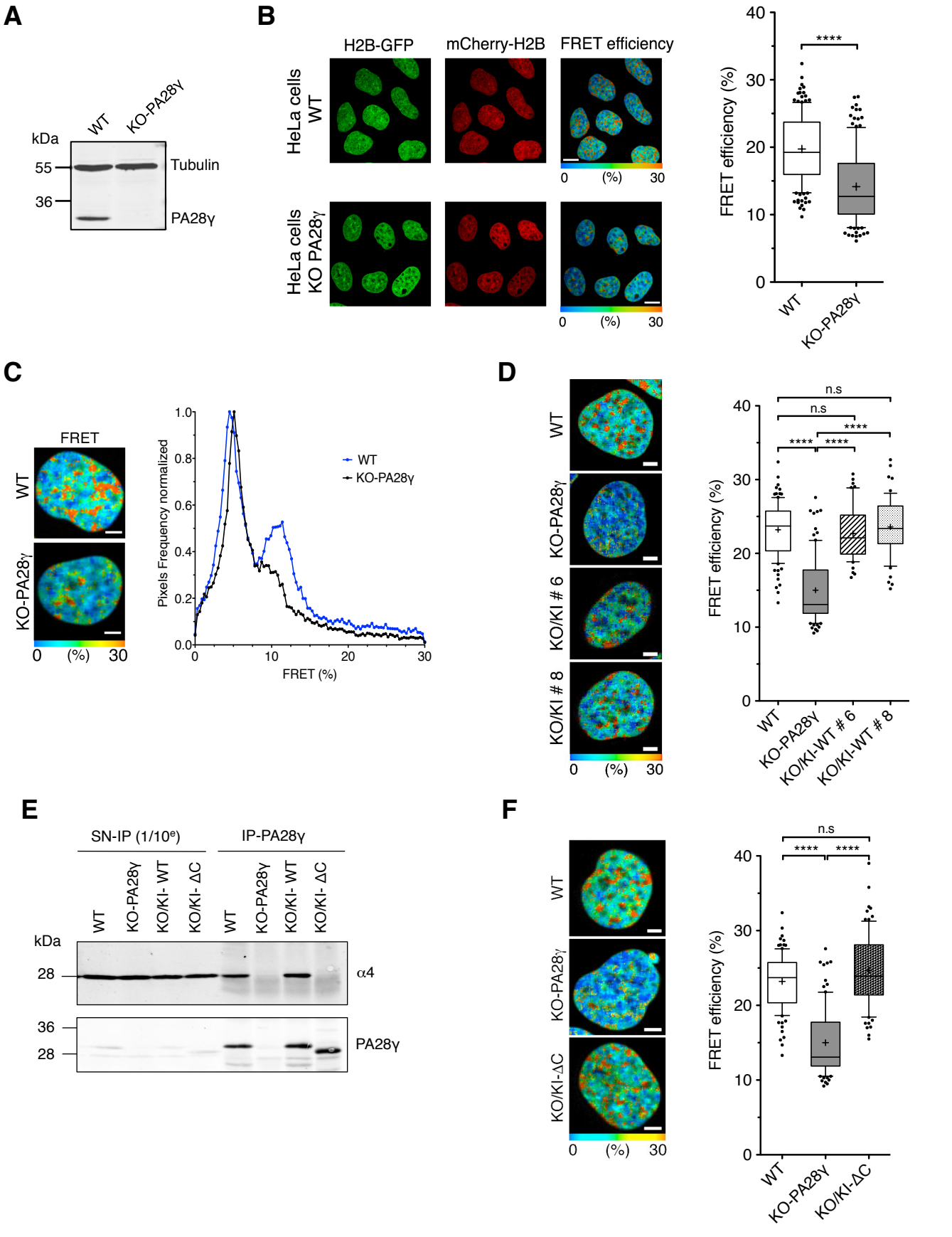
A
WT
KO-PA28γ
kDa
55
36
Tubulin
PA28γ
B
H2B-GFP
mCherry-H2B
FRET efficiency
HeLa cells WT
HeLa cells KO PA28γ
0
(%)
30
FRET efficiency (%)
40
30
20
10
0
****
WT
KO-PA28γ
C
FRET
WT
KO-PA28γ
0
(%)
30
Pixels Frequency normalized
1.0
0.8
0.6
0.4
0.2
0.0
0
10
20
30
FRET (%)
WT
KO-PA28γ
D
WT
KO-PA28γ
KO/KI # 6
KO/KI # 8
0
(%)
30
n.s
n.s
****
****
****
FRET efficiency (%)
40
30
20
10
0
WT
KO-PA28γ
KO/KI-WT # 6
KO/KI-WT # 8
E
SN-IP (1/10e)
IP-PA28γ
WT
KO-PA28γ
KO/KI- WT
KO/KI- ΔC
kDa
28
36
28
α4
PA28γ
F
WT
KO-PA28γ
KO/KI-ΔC
0
(%)
30
n.s
****
****
FRET efficiency (%)
40
30
20
10
0
WT
KO-PA28γ
KO/KI-ΔC

Figure 4

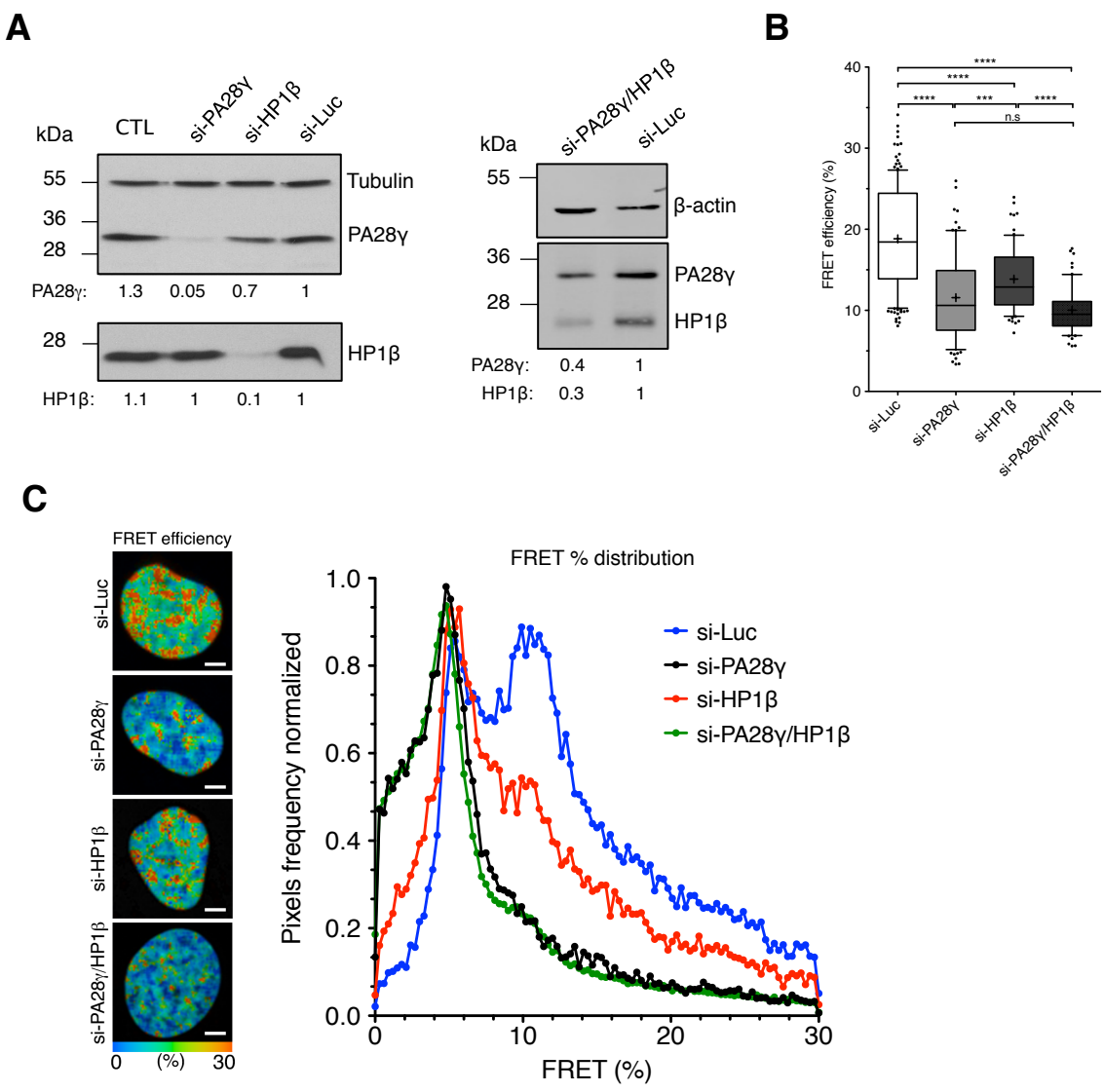
A
kDa
CTL
si-PA28γ
si-HP1β
si-Luc
55
36
28
Tubulin
PA28γ
PA28γ: 1.3 0.05 0.7 1
28
HP1β
HP1β: 1.1 1 0.1 1
kDa
si-PA28γ/HP1β
si-Luc
55
β-actin
36
28
PA28γ
HP1β
PA28γ: 0.4 1
HP1β: 0.3 1
B
FRET efficiency (%)
40
30
20
10
0
****
****
****
***
****
n.s
si-Luc
si-PA28γ
si-HP1β
si-PA28γ/HP1β
C
FRET efficiency
si-Luc
si-PA28γ
si-HP1β
si-PA28γ/HP1β
0
(%)
30
FRET % distribution
Pixels frequency normalized
1.0
0.8
0.6
0.4
0.2
0.0
0
10
20
30
FRET (%)
si-Luc
si-PA28γ
si-HP1β
si-PA28γ/HP1β

Figure 5

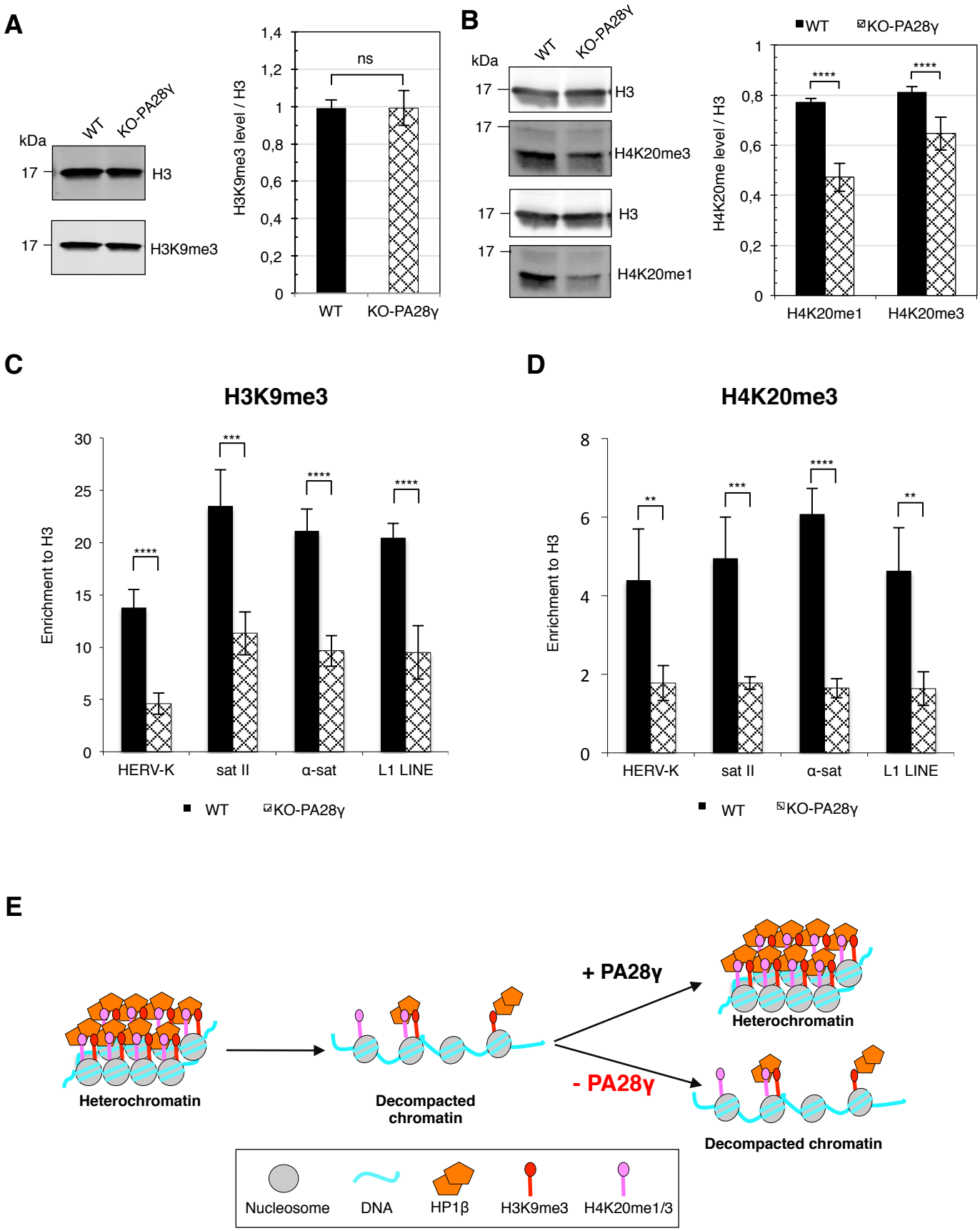
A
kDa
WT
KO-PA28γ
17
H3
17
H3K9me3
H3K9me3 level / H3
ns
1,4
1,2
1
0,8
0,6
0,4
0,2
0
WT
KO-PA28γ
B
kDa
WT
KO-PA28γ
17
H3
17
H4K20me3
17
H3
17
H4K20me1
WT
KO-PA28γ
H4K20me level / H3
****
****
1
0,8
0,6
0,4
0,2
0
H4K20me1
H4K20me3
C
H3K9me3
Enrichment to H3
30
25
20
15
10
5
0
***
****
****
****
HERV-K
sat II
α-sat
L1 LINE
WT
KO-PA28γ
D
H4K20me3
Enrichment to H3
8
6
4
2
0
**
***
****
**
HERV-K
sat II
α-sat
L1 LINE
WT
KO-PA28γ
E
Heterochromatin
Decompacted chromatin
+ PA28γ
- PA28γ
Heterochromatin
Decompacted chromatin
Nucleosome
DNA
HP1β
H3K9me3
H4K20me1/3

Figure 6

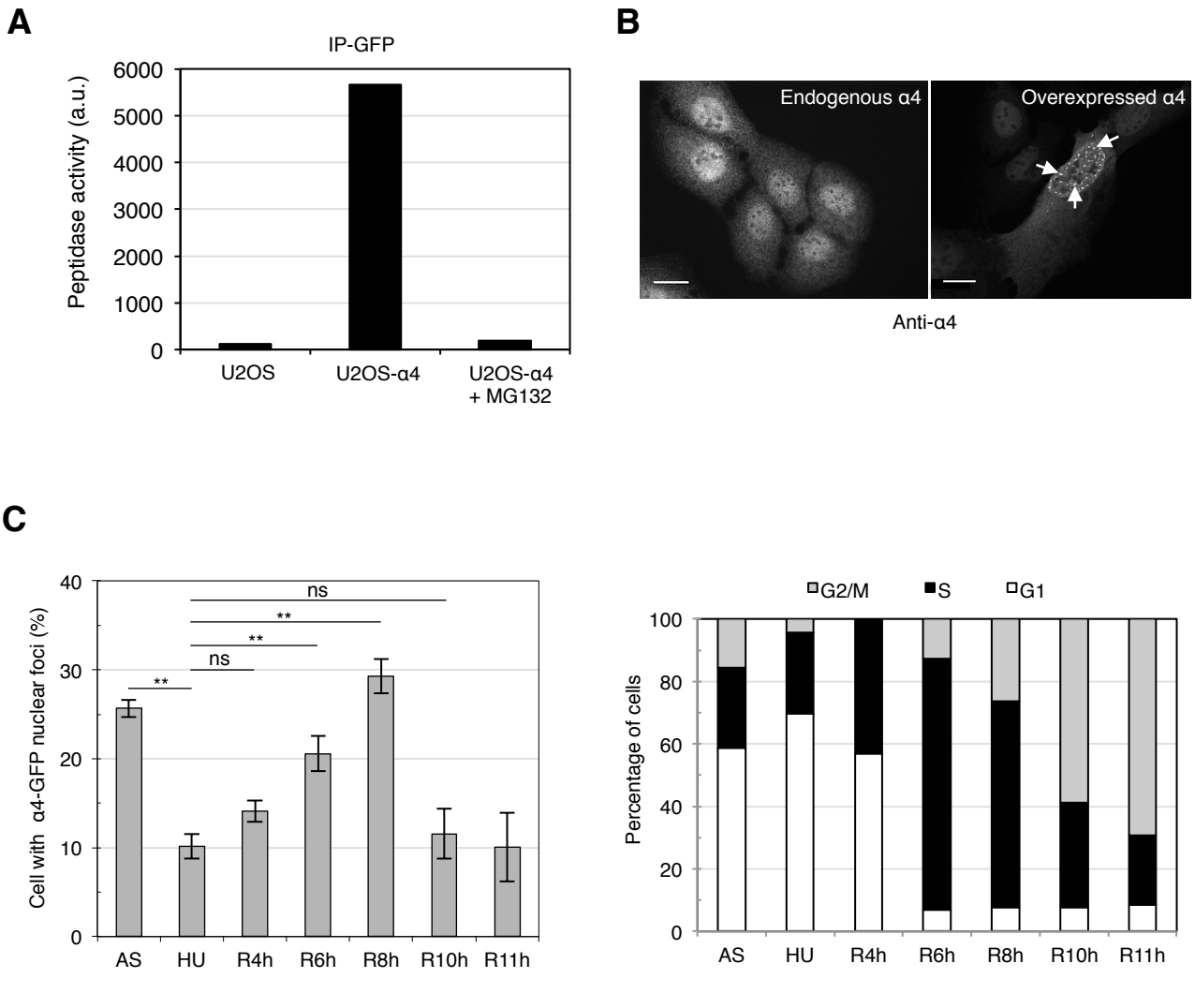
A
IP-GFP
Peptidase activity (a.u.)
6000
5000
4000
3000
2000
1000
0
U2OS
U2OS-α4
U2OS-α4
+ MG132
B
Endogenous α4
Overexpressed α4
Anti-α4
C
Cell with α4-GFP nuclear foci (%)
40
30
20
10
0
ns
**
**
**
ns
AS
HU
R4h
R6h
R8h
R10h
R11h
G2/M
S
G1
Percentage of cells
100
80
60
40
20
0
AS
HU
R4h
R6h
R8h
R10h
R11h

Figure S1

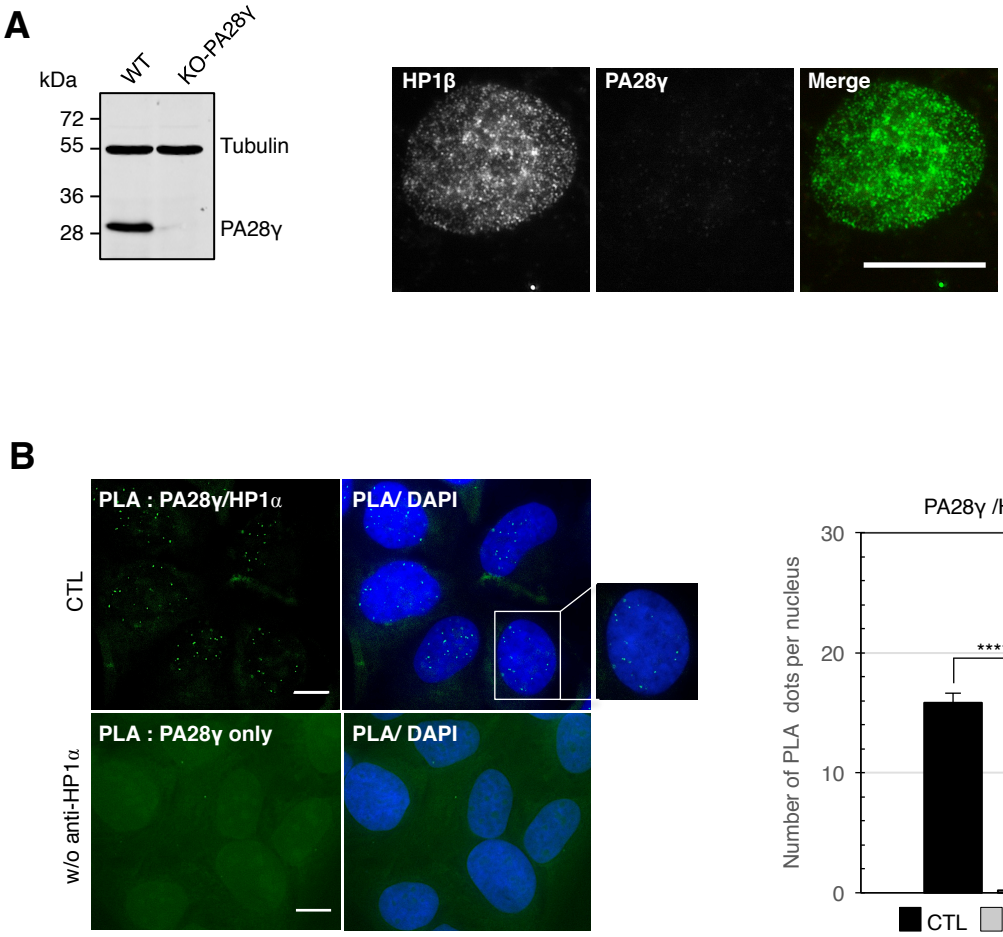
A
kDa
WT
KO-PA28γ
72
55
Tubulin
36
28
PA28γ
HP1β
PA28γ
Merge
B
CTL
w/o anti-HP1α
PLA : PA28γ/HP1α
PLA/ DAPI
PLA : PA28γ only
PLA/ DAPI
PA28γ /HP1α
Number of PLA dots per nucleus
30
20
10
0
****
CTL
w/o anti-HP1α
C
kDa
WT
KO-PA28γ
KO-PIP30
36
28
anti-PA28γ
36
28
anti-PIP30
WT
KO-PIP30
PLA : HP1β/PA28γ
PLA : HP1β/PA28γ
PLA + DAPI
PLA + DAPI
Number of PLA dots per nucleus
100
90
80
70
60
50
40
30
20
10
0
****
ns
WT
KO-PIP30
KO-PA28γ

Figure S2

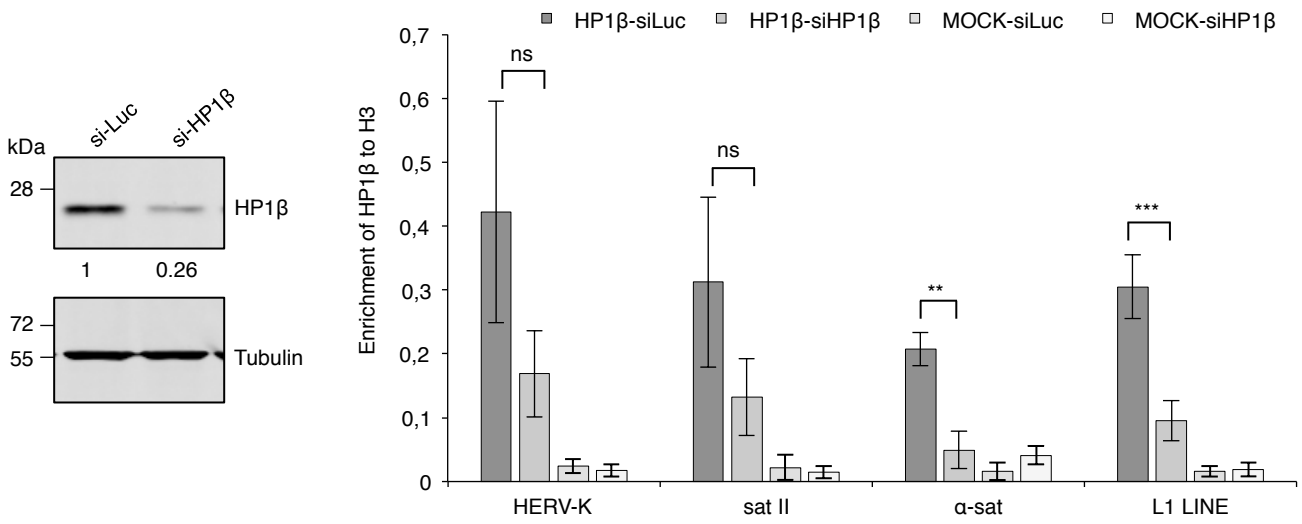
si-Luc
si-HP1β
kDa
28
HP1β
1
0.26
72
55
Tubulin
HP1β-siLuc
HP1β-siHP1β
MOCK-siLuc
MOCK-siHP1β
Enrichment of HP1β to H3
0,7
0,6
0,5
0,4
0,3
0,2
0,1
0
ns
ns
**
***
HERV-K
sat II
α-sat
L1 LINE

Figure S3

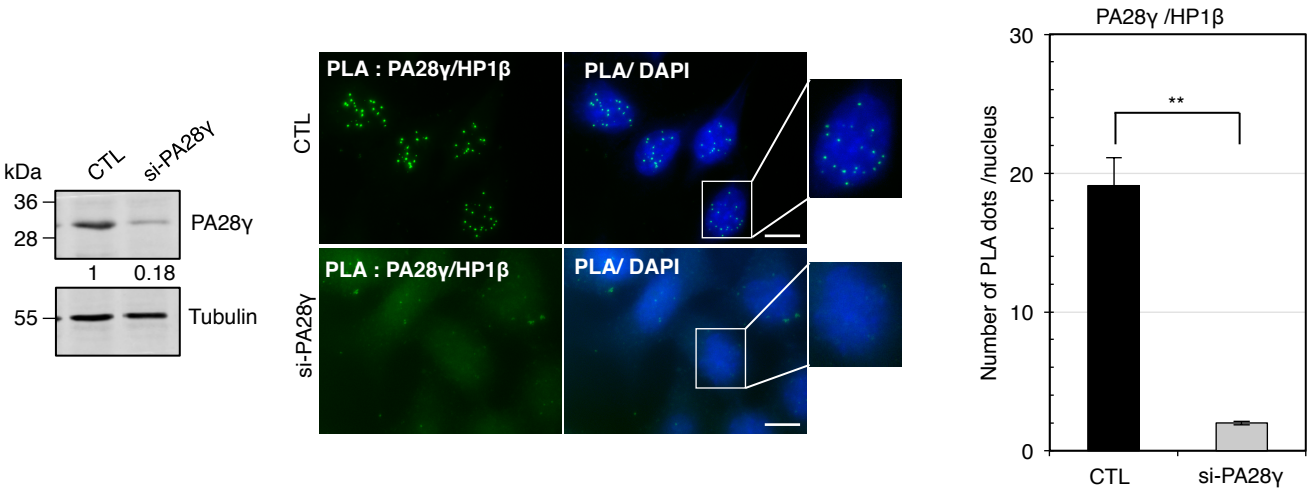
kDa
CTL
si-PA28γ
36
28
PA28γ
1
0.18
55
Tubulin
CTL
si-PA28γ
PLA : PA28γ/HP1β
PLA/ DAPI
PLA : PA28γ/HP1β
PLA/ DAPI
PA28γ /HP1β
Number of PLA dots /nucleus
30
20
10
0
**
CTL
si-PA28γ

Figure S4

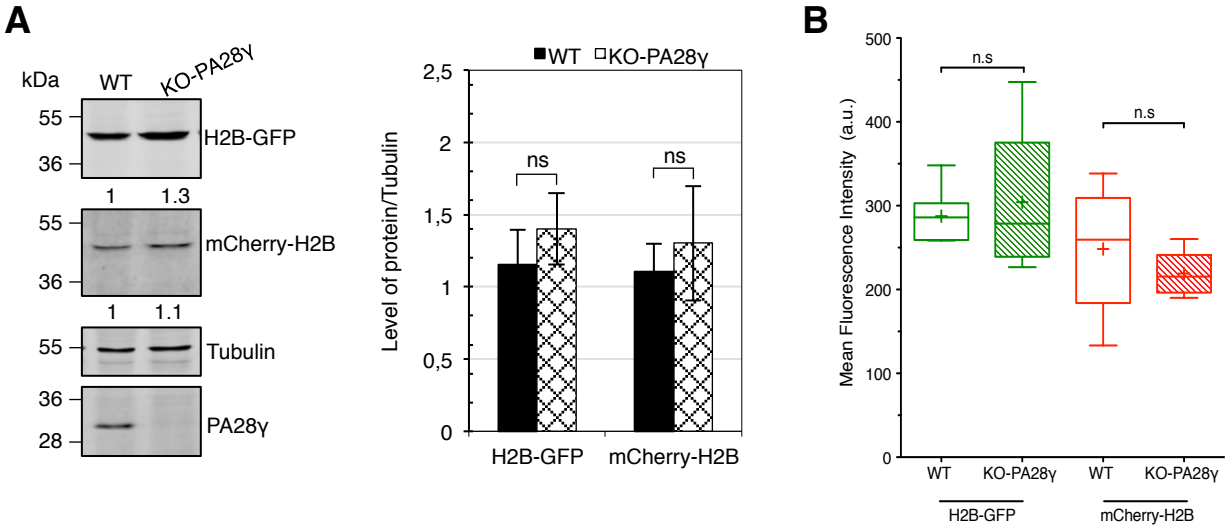
A
kDa
WT
KO-PA28γ
55
36
H2B-GFP
1
1.3
55
36
mCherry-H2B
1
1.1
55
Tubulin
36
28
PA28γ
WT
KO-PA28γ
Level of protein/Tubulin
2,5
2
1,5
1
0,5
0
ns
ns
H2B-GFP
mCherry-H2B
B
Mean Fluorescence Intensity (a.u.)
500
400
300
200
100
0
n.s
n.s
WT
KO-PA28γ
WT
KO-PA28γ
H2B-GFP
mCherry-H2B

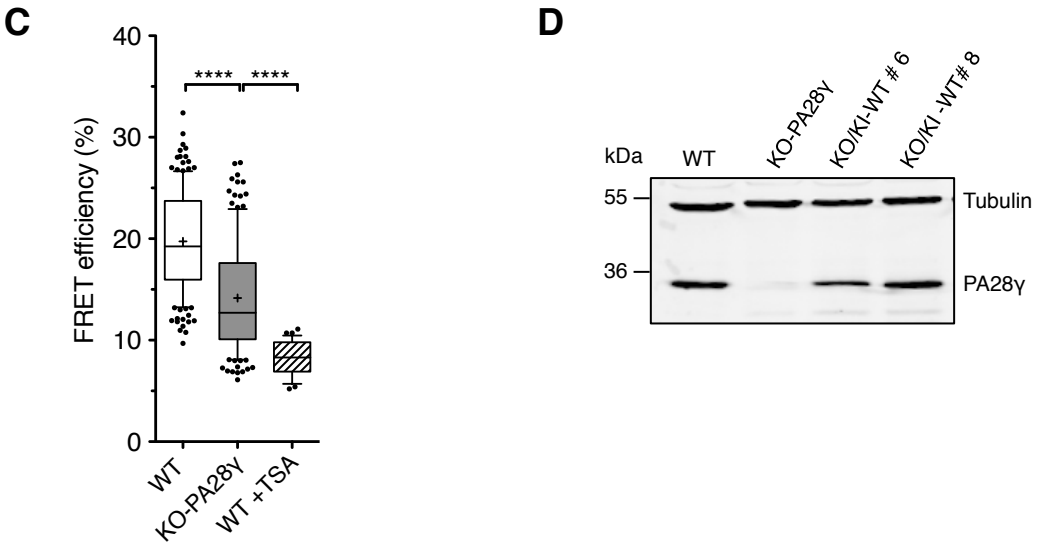
C
FRET efficiency (%)
40
30
20
10
0
****
****
WT
KO-PA28γ
WT +TSA
D
kDa
WT
KO-PA28γ
KO/KI-WT#6
KO/KI -WT#8
55
36
Tubulin
PA28γ

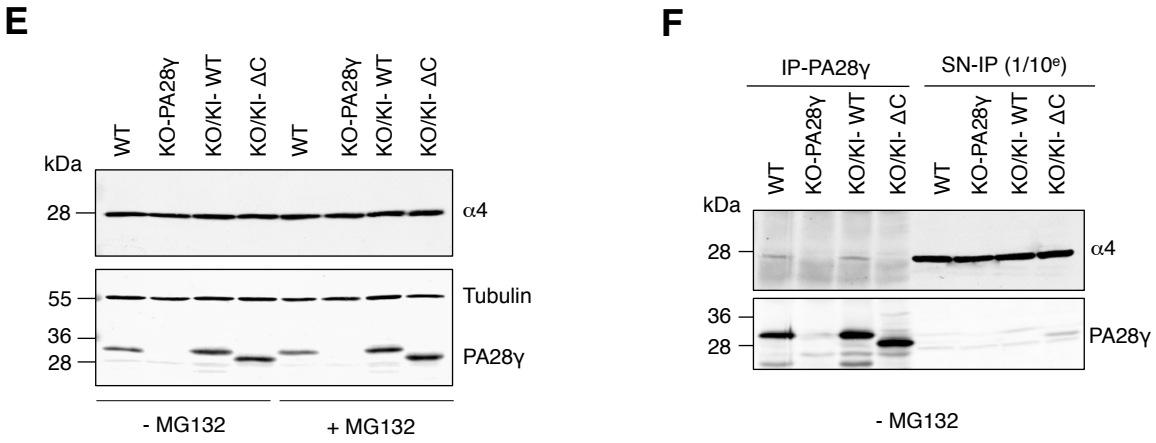
E
WT
KO-PA28γ
KO/KI- WT
KO/KI- ΔC
WT
KO-PA28γ
KO/KI- WT
KO/KI- ΔC
kDa
28
α4
55
36
28
Tubulin
PA28γ
- MG132
+ MG132
F
IP-PA28γ
SN-IP (1/10e)
WT
KO-PA28γ
KO/KI- WT
KO/KI- ΔC
WT
KO-PA28γ
KO/KI- WT
KO/KI- ΔC
kDa
28
α4
36
28
PA28γ
- MG132

Figure S5

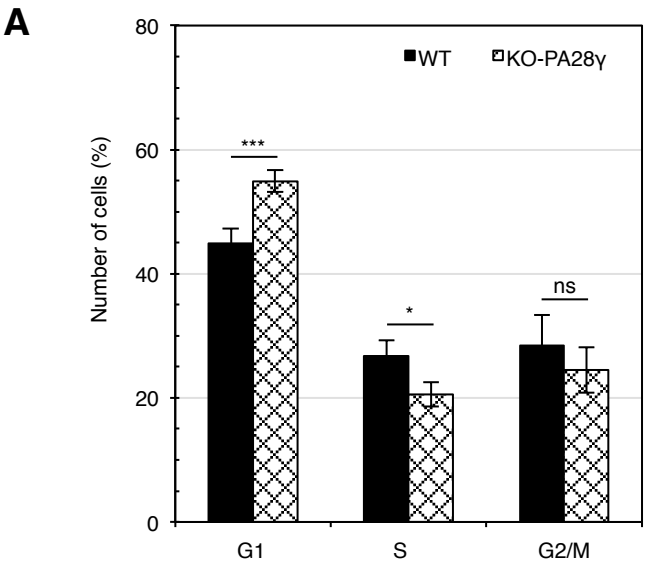
A
WT
KO-PA28γ
Number of cells (%)
80
60
40
20
0
***
*
ns
G1
S
G2/M

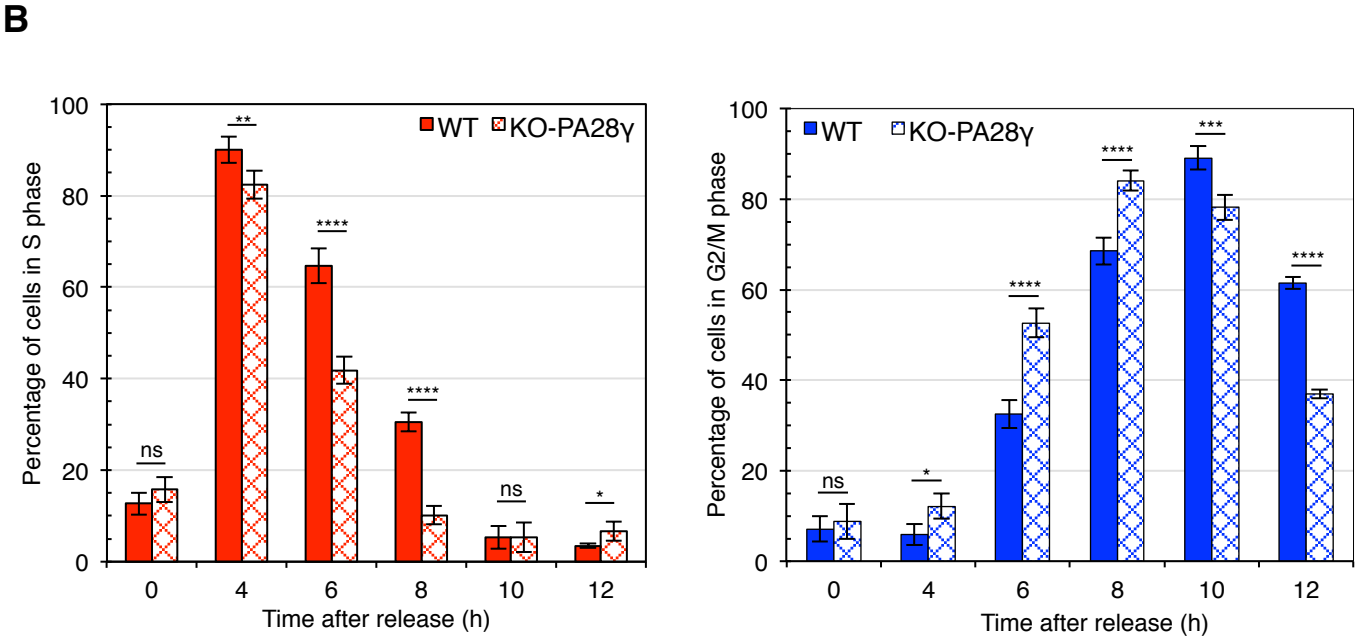
B
WT
KO-PA28γ
Percentage of cells in S phase
Percentage of cells in G2/M phase
Time after release (h)
0
4
6
8
10
12
ns
**
****
*
***

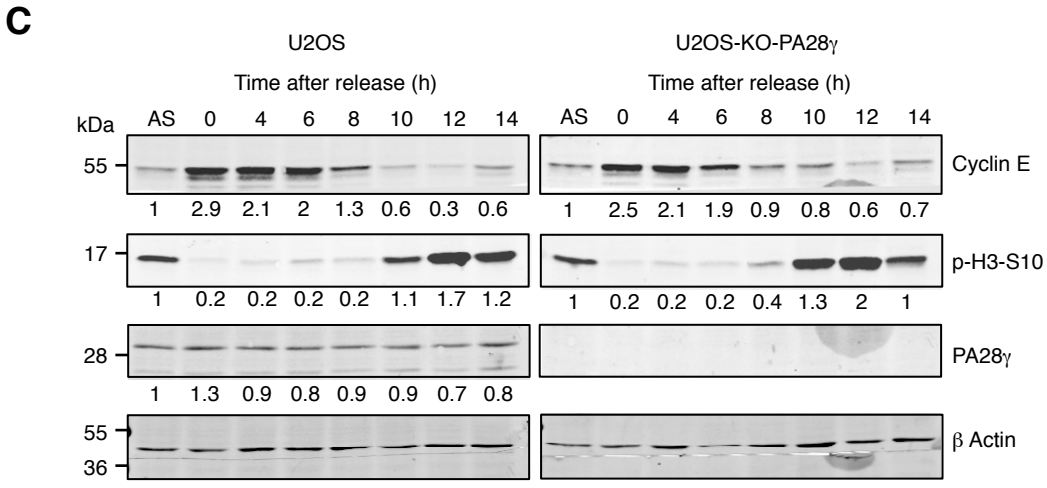
C
U2OS
U2OS-KO-PA28γ
Time after release (h)
kDa
AS
0
4
6
8
10
12
14
55
17
28
36
Cyclin E
p-H3-S10
PA28γ
β Actin
1 2.9 2.1 2 1.3 0.6 0.3 0.6
1 2.5 2.1 1.9 0.9 0.8 0.6 0.7
1 0.2 0.2 0.2 0.2 1.1 1.7 1.2
1 0.2 0.2 0.2 0.4 1.3 2 1
1 1.3 0.9 0.8 0.9 0.9 0.7 0.8

Figure S6

Table 1: *p* values of the figure 6C-D (ChIP)

	T-test (H3K9me3/H3) U2OS *vs* KO PA28γ	T-test (H4K20me3/H3) U2OS *vs* KO PA28γ
HERV-K	6,47871E-06	0,009044059
α sat	0,00014585	0,001004765
Sat II	8,6538E−06	1,37015E−05
L1 LINE	2,80855E-05	0,002330735

Table 2: *p* values of the figure S1C

	AS	HU	R4h	R6h	R8h	R10h	R11h
AS		0,0011	0,0099	0,0723	0,0264	0,0047	0,0127
HU			0,1957	0,0017	0,0013	0,7166	>0.9999
R4h				0,0938	0,0124	0,827	0,6832
R6h					0,0286	0,021	0,021
R8h						0,0011	0,0041
R10h							0,4511
R11h							

Table 3: *p* values of the figure S3 (ChIP)

	T-test (si-Luc *vs* si-HP1β)
HERV-K	0,057078569
Sat II	0,066693611
α–sat	0,005250998
L1 LINE	0,000382203

Table 4: *p* values of the figure S6 (determined with the 2-way ANOVA)

	Time after release (hours)					
PHASE	0	4	6	8	10	12
G1	0.9919	0.8713	0.5848	0.2726	0.0002	< 0.0001
S	0.6759	0.0052	< 0.0001	< 0.0001	> 0.9999	0.0377
G2/M	0.9946	0.0187	< 0.0001	< 0.0001	< 0.0002	< 0.0001